Article
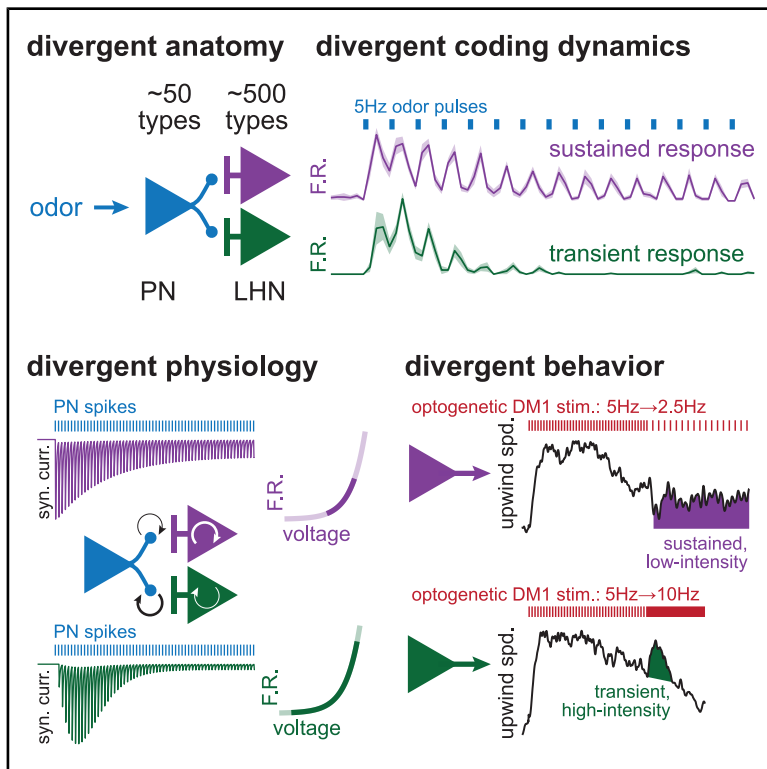
Divergent synaptic dynamics originate parallel pathways for computation and behavior in an olfactory circuit

Graphical abstract

Highlights

- Lateral horn neurons (LHNs) in *Drosophila* exhibit divergent odor-coding dynamics

- This originates via target-neuron-specific short-term plasticity of synaptic inputs

- Plasticity depends, in part, on presynaptic calcium signaling via Unc13B

- Sustained and transient LHNs contribute to sustained and transient behavior

Authors

Hyong S. Kim,
Gustavo Madeira Santana,
Gizem Sancer, Thierry Emonet,
James M. Jeanne

Correspondence

james.jeanne@yale.edu

In brief

Kim et al. investigate how the *Drosophila* olfactory system dynamically transforms odor information. They discover that distinct synaptic dynamics from individual projection neurons underlie different odor-coding dynamics in different lateral horn neurons (LHNs). Transient and sustained LHNs make corresponding dynamic contributions to behavior.

Current Biology

CellPress

Article

Divergent synaptic dynamics originate parallel pathways for computation and behavior in an olfactory circuit

Hyong S. Kim,[1] Gustavo Madeira Santana,[2,5] Gizem Sancer,[1,4] Thierry Emonet,[2,4,5] and James M. Jeanne[1,2,3,4,6,*]

[1]Department of Neuroscience, Yale University School of Medicine, New Haven, CT 06510, USA
[2]Department of Molecular, Cellular, and Developmental Biology, Yale University, New Haven, CT 06511, USA
[3]Kavli Institute for Neuroscience, Yale University School of Medicine, New Haven, CT 06510, USA
[4]Wu-Tsai Institute, Yale University, New Haven, CT 06510, USA
[5]Quantitative Biology Institute, Yale University, New Haven, CT 06511, USA
[6]Lead contact
*Correspondence: james.jeanne@yale.edu
https://doi.org/10.1016/j.cub.2025.05.051

SUMMARY

To enable diverse sensory processing and behavior, central circuits use divergent connectivity to create parallel pathways. However, linking synaptic and cellular mechanisms to the circuit-level segregation of computation has been challenging. Here, we investigate the generation of parallel processing pathways in the *Drosophila* olfactory system, where glomerular projection neurons (PNs) diverge onto many lateral horn neurons (LHNs). We compare the effects of a single PN's activity on two of its target LHNs. One LHN type generates sustained responses to odor and adapts divisively. The other generates transient responses and adapts subtractively. The distinct odor-coding dynamics originate from differences in the dynamics of PN synapses targeting each LHN type. Sustained LHN responses arise from synapses that recover from depression quickly enough to maintain ongoing transmission. Divisive adaptation is due to slow cellular gain control implemented by the Na^+/K^+ ATPase in the postsynaptic neuron. Transient LHN responses arise from synapses that recover from depression too slowly to maintain ongoing transmission but that also facilitate when PN spike rate increases. Interfering with facilitation via the calcium buffer EGTA or interfering with the presynaptic priming factor Unc13B diminishes the magnitude of initial transient responses. Subtractive adaptation is due to the nonlinearity imposed by the spike threshold in the postsynaptic neuron. Transient LHNs make corresponding transient contributions to behavioral odor attraction in walking flies, whereas sustained LHNs may make sustained, but nuanced, contributions. Subcellular presynaptic specialization is thus a compact and efficient way to originate parallel information streams for specialized computation and behavior.

INTRODUCTION

Many stages of sensory processing in the brain are characterized by a limited number of neuron types that expand onto larger and more diverse downstream populations. This architecture allows for greater specialization later in sensory processing.[1] For instance, specialized transient and sustained representations emerge downstream of receptor neurons in both vision and olfaction.[2–4]

The elemental unit of expansion is divergence, where the axon of a single presynaptic neuron connects to multiple postsynaptic targets. Even within that one axon, specialization can already begin when presynaptic short-term plasticity differs for different target neurons.[5–11] Although this subcellular specification of plasticity is widespread throughout the brain, we do not know how it contributes to different computation and behavior.

Addressing this issue involves three questions. First, how does sensory coding diversify downstream of a single neuron? Second, what are the cellular and subcellular molecular differences

that produce this diversity? Finally, how do the different downstream neurons contribute to behavioral function?

To answer these questions, one would ideally identify individual neurons that form distinct synapse types onto different target neurons, directly compare their sensory coding properties *in vivo*, and genetically perturb them while measuring physiology and behavior. A useful experimental system for this purpose is the *Drosophila* lateral horn, a compact olfactory network with stereotyped synaptic connections.[12–15] Antennal lobe projection neurons (PNs) gather input from peripheral olfactory receptor neurons (ORNs), reliably encoding temporal odor patterns and sending their outputs to the lateral horn.[16–18] There, each PN axon diverges to form excitatory synaptic connections onto dozens of anatomically distinct types of lateral horn neurons (LHNs),[3,12–14,19,20] some of which instruct behavioral attraction or aversion.[21,22]

We aimed to understand how divergence from PNs to LHNs creates parallel channels for computation and behavior. We identify two LHN types that receive input from the same PNs yet differ

in the transience of their responses to odor. One generates sustained responses and adapts divisively (i.e., adjusts its gain by scaling its tuning curve). The other generates transient responses and adapts subtractively (i.e., adjusts its sensitivity by shifting its tuning curve). We then trace the mechanisms that enable this divergent functionality, finding that it originates, in part, from target-neuron-specific synaptic dynamics within the axon of a single PN. Ultimately, this circuitry enables separate control of sustained and transient components of odor-evoked upwind walking and may underlie a more general motif for independent regulation of behavioral dynamics. Overall, our results provide a mechanistic understanding of how an elementary motif of neuronal architecture—divergence—creates temporally diverse computation and behavior.

RESULTS

In this study, we focused on processing downstream of the DM1 glomerulus because it makes substantial contributions to behavioral attraction[23,24] and the DM1 PN has good genetic access for targeted electrophysiology and manipulation.[25] DM1 PN axons connect to many different LHN types (Figures S1A and S1B). Based on pilot experiments, we chose to focus on two LHN types, called "PD2a1/b1" and "PV5a1," because they differed in the transience of their responses to odor (Figures 1A, 1B, S1C, and S1D). For simplicity, we refer to these types as "LHN1" and "LHN2," respectively.

Sustained and transient representations of odor in different LHN types

Based on prior work,[26] we identified a low concentration (1×10^{-6} dilution) of ethyl acetate to activate DM1 PNs without activating other PN types (Figures 1C and S2). We delivered odor in repeated 40 ms pulses, which caused DM1 spike rates to adapt modestly over time (Figure 1C). Increasing the pulse frequency from 1 to 10 Hz (all with 40 ms pulses) delivered more odor molecules per second, increasing DM1 spike rates (Figure 1D). Behavioral responses begin to integrate over time for odor dynamics above 1 Hz,[27,28] so these pulsed stimuli provided a convenient way to modulate average stimulus intensity on a timescale of 1 s, while maintaining private DM1 activation.

Using these odor stimuli, we then compared the responses of LHN1 and LHN2. Prior to stimulus onset, LHN1 exhibited higher spontaneous spike rates than LHN2, which was almost completely silent (Figure 1E). During the first 1 s of 5 Hz stimulation, both LHNs exhibited similar transient spike rates (Figures 1E and 1F). After adaptation to 10 or more seconds of constant frequency odor stimulation, LHN1 maintained positive "steady-state" spike rates, whereas LHN2 spike rates returned to nearly zero (Figures 1E and 1F). The distinction in transience also occurred for odors that activate different PN inputs, odors at higher (non-private) concentrations, and odors delivered continuously (Figure S3). Pharmacological blockers of synaptic inhibition did not impair the transience of LHN2 (Figure S3).

The differences in steady-state activity between LHN types suggested fundamental differences in adaptation. To investigate this quantitatively, we delivered 20 s of odor at 5 Hz to drive adaptation into steady state and then switched to a "test" frequency (1–10 Hz; Figure 1G). We measured transient responses

to each test stimulus and compared them with responses without adaptation. Adaptation scaled the gain of LHN1's tuning curve (i.e., divisive adaptation), centered around the adapted odor frequency (Figure 1H). This meant that LHN1 maintained responses to ongoing odors and signaled both stimulus increases and decreases. In contrast, adaptation shifted LHN2's tuning curve along the horizontal axis (i.e., subtractive adaptation), positioning it *above* the adapted odor frequency (Figure 1I; note that LHN2 also exhibited some gain modulation). LHN2 was therefore unresponsive to ongoing odors and responded only transiently to stimulus increases.

Adapting to lower stimulus frequencies led to smaller but qualitatively similar changes in tuning curves (Figures 1H, 1I, and S4A–S4F). Stimulation with methyl acetate (to privately activate the DM4 PN) yielded similar results (Figures S4G–S4M), suggesting the distinctions in adaptation are consistent across glomerular inputs. Overall, these data show that LHN1 and LHN2 adapt in different ways to emphasize distinct temporal features of dynamic odor patterns.

Differences in LHN adaptation originate from differences in filtering of PN spikes

Under our stimulus conditions, the single DM1 PN is the sole source of odor-evoked excitation to LHN1 and LHN2. We thus sought to compare how these two LHN types process the same DM1 spikes. Focusing on the 5–10 Hz stimulus (because the effects of adaptation were strongest), we used dynamic linear filter models to predict LHN membrane potentials from the sequence of DM1 spike times (STAR Methods). We fit separate filters for three conditions: the initial unadapted response to 5 Hz odor pulses ("U5"), the adapted responses to 5 Hz pulses ("A5"), and the adapted response to 10 Hz odor pulses ("A10"; Figure 2A). In all conditions, filters for LHN1 were shorter in duration than the filters for LHN2 (Figures 2B and 2C).

We then asked how the filter shapes differed across adaptation conditions. Adaptation to 5 Hz odor pulses reduced the width of the LHN1 filter without changing its amplitude (Figures 2B and 2C). In contrast, adaptation reduced the amplitude of the LHN2 filter without changing its width (Figures 2B and 2D). When the odor pulse rate increased to 10 Hz, the LHN2 filter amplitude increased, partially restoring its original unadapted amplitude (Figures 2B and 2D). Thus, adaptation reduces the impact of DM1 spikes on the membrane potentials of both LHN1 and LHN2, but in different ways: it decreases the duration of LHN1 responses but decreases the magnitude of LHN2 responses.

Adaptation could also directly alter LHN excitability. To assess this, we investigated the relationship between membrane voltage and spike rate for each LHN type. Spike rate largely followed an expansive, exponential function of voltage in each type, as expected from a canonical spike threshold (Figures 2E and 2F). A single function could account for spike rates in all conditions for each LHN type, although the excitability of both types was elevated at the start of the U5 and A10 conditions (reflecting the "dynamic" spike threshold known to exist in LHNs[29,30]). Altogether, this indicates that adaptation had minimal direct impact on LHN excitability.

The effects of adaptation on membrane voltage nonetheless interacted with spike thresholds differently in each LHN type.

Current Biology
Article

CellPress
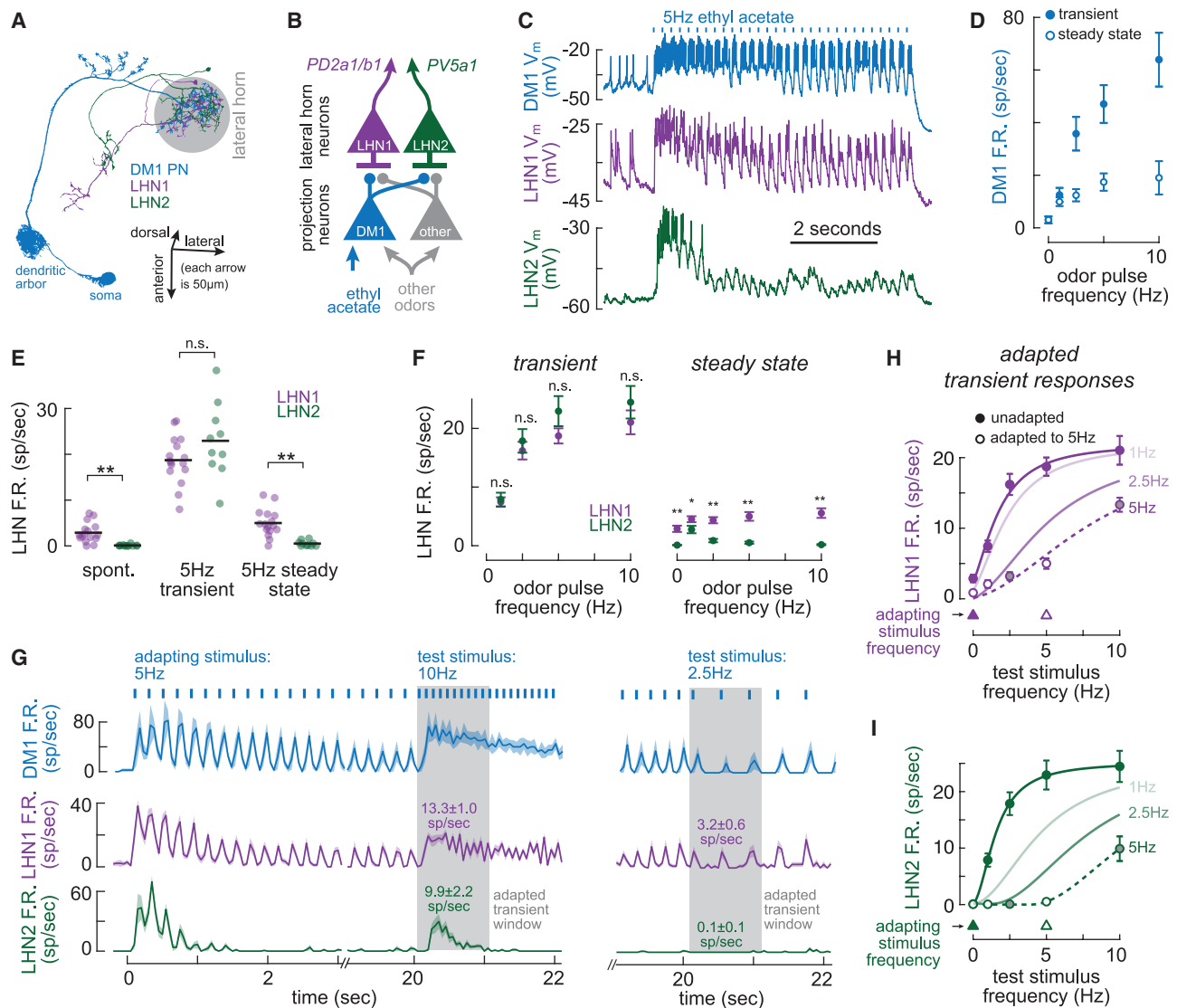
Figure 1. Parallel representation of sustained and transient odor information

(A) Anatomy (from hemibrain connectome) of the primary neuron types investigated in this study.

(B) Schematic of the microcircuit of DM1, LHN1, and LHN2. Low-concentration ethyl acetate activates DM1 without activating other PNs (see also Figure S2). DM1 outputs diverge onto both LHN1 and LHN2, which both also receive inputs from other PN types.

(C) Representative traces of current clamp recordings of each neuron type in response to 30 pulses (40 ms each) of ethyl acetate repeated at 5 Hz. LHN1 maintains spikes for each pulse; LHN2 spikes rapidly adapt away.

(D) Mean (±SEM) firing rates of DM1 ($n = 4$) during the initial transient response (first 1 s) and the steady-state response (after at least 9 s of stimulation at constant frequency).

(E) Comparison of spontaneous, transient, and steady-state firing rates (at 5 Hz stimulation) for LHN1 ($n = 16$) and LHN2 ($n = 10$–12). t tests, **$p < 2 \times 10^{-4}$.

(F) Mean (±SEM) transient and steady-state firing rates for different odor stimulus rates for LHN1 ($n = 16$) and LHN2 ($n = 10$–12). t tests, *$p < 0.05$; **$p < 3 \times 10^{-4}$.

(G) Mean (±SEM) peristimulus time histograms (PSTHs) of spike rates in DM1 ($n = 4$), LHN1 ($n = 10$), and LHN2 ($n = 7$). The stimulus is ethyl acetate pulsed at 5 Hz for 20 s prior to switching to either 10 (left) or 2.5 Hz (right). Note the truncated x axes. Gray shading denotes 1-s analysis window for computing mean adapted transient spike rates (corresponding to shaded circles in H and I).

(H) Mean (±SEM) ethyl acetate responses for LHN1 ($n = 9$–16) for a range of stimulus frequencies without adaptation (solid circles) and adapted to 5 Hz (open circles). Gray shaded circles correspond to shaded regions in the representative PSTHs in (G). Solid curve is fit to unadapted spike rates, and then only its offset and gain were adjusted to fit the adapted data (dashed curve; STAR Methods). Adapting pulse frequencies are plotted in triangles at bottom. Lighter purple curves are the corresponding fits after adaptation to 2.5 Hz or 1 Hz (data shown in Figure S4).

(I) Same as (H) but for LHN2 ($n = 6$–16).

See also Figures S1–S5.
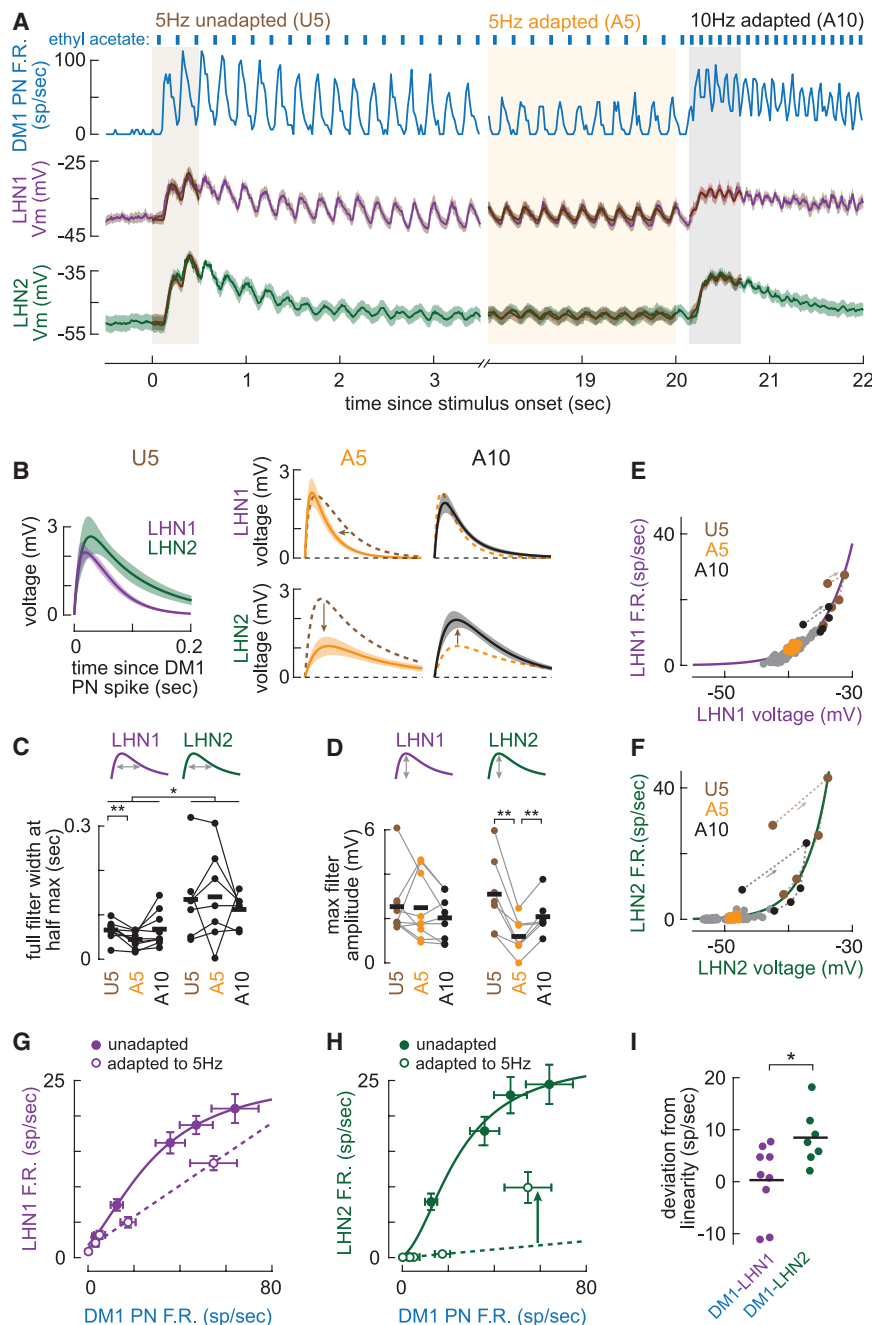
Figure 2. Adaptation alters how LHN1 and LHN2 filter DM1 spikes

(A) Top: mean PSTH of DM1 PNs ($n = 4$) in response to the 5–10 Hz ethyl acetate stimulation. Middle and bottom: mean (±SEM) membrane voltage (V_m) in response to the same stimulus for LHN1 ($n = 10$) and LHN2 ($n = 7$), respectively. Rectangular shaded areas denote the three model fitting windows. Superimposed brown traces are the mean (±SEM) linear model predictions within each fitting window. x axis is truncated for display purposes.

(B) Left: mean (±SEM) of filters fit to each LHN1 and LHN2 recording during the unadapted 5 Hz window (U5). Center: mean (±SEM) of filters fit to each LHN1 and LHN2 recording during the adapted 5 Hz window (A5). Brown dashed line denotes the mean U5 filter fits (from left). Right: mean (±SEM) of filters fit to each LHN1 and LHN2 recording during the adapted 10 Hz window (A10). Orange dashed line denotes the mean A5 filter fits (from center). Timescale is identical for all traces.

(C) Comparison of filter widths in each fitting window for LHN1 and LHN2. t tests, *$p < 0.05$; **$p < 0.007$.

(D) Comparison of filter amplitudes in each fitting window for LHN1 and LHN2. t tests, **$p < 0.006$.

(E) Relationship between mean LHN1 voltage and spike rate in 200 ms bins over the full response to the 5–10 Hz stimulus. Each point denotes a single bin. Points within each of the three fitting windows are colored correspondingly and are connected by dashed lines. The arrow points in the direction of time for the U5 and A10 windows. The first bin within these two windows is more excitable, likely due to the dynamic threshold in LHNs.

(F) Same as (E) but for LHN2.

(G) Input-output functions relating mean (±SEM) DM1 ($n = 4–8$) and LHN1 ($n = 9–16$) firing rates for unadapted transient responses (solid circles) and adapted transient responses (open circles). Dashed line is a linear fit to the leftmost 4 points, which is a good prediction of the rightmost point.

(H) Same as (G) but for LHN2 ($n = 7–12$). Note that the linear fit substantially underestimates the rightmost point, indicating a deviation from linearity (arrow).

(I) Comparison of deviations from linearity, as illustrated by the arrow in (H). Each point denotes one LHN recording. t test, *$p = 0.023$.

See also Figure S5.

LHN1 traversed a narrow range of voltages during the 5–10 Hz stimulus and only minimally engaged the nonlinearity. Adaptation in LHN1 thus led to voltages that were mostly above threshold, with corresponding spike rates following an approximately linear function of DM1 spike rates (Figure 2G). Adaptation in LHN2, however, led to a wider range of voltages that broadly engaged the exponential nonlinearity, with corresponding spike rates following an expansive nonlinear function of DM1 spike rate (Figures 2H and 2I). Together, this explains how LHN2 adapts so completely: when DM1 spike rate increases, those spikes depolarize LHN2 strongly enough to substantially surpass spike

threshold. But when DM1 spike rate is constant or decreasing, those spikes only weakly depolarize LHN2, keeping it securely below spike threshold.

Adaptation is more input specific in LHN2 than in LHN1

Synaptic and cellular mechanisms can both implement adaptation but have different signatures.[31] Synaptic adaptation is generally input specific, meaning that excitation from one synapse does not cross-adapt excitation from another. Cellular adaptation is generally input generic, meaning that excitation from any synapse can cross-adapt excitation from another.

Current Biology
Article

🔹 CellPress

To compare the input specificity of adaptation in LHN1 and LHN2, we took advantage of the fact that both also receive input from the DM4 PN (Figures S1A and S1B), which is privately activated by methyl acetate (Figure S2). We thus tested whether adaptation induced by ethyl acetate (via DM1) affects subsequent LHN responses to methyl acetate (via DM4). This form of cross-adaptation was significantly larger in LHN1 than in LHN2 (and not evident in DM4 PNs; Figure S5). Thus, adaptation likely occurs via a cellular mechanism in LHN1 and via a synaptic mechanism in LHN2.

PN-LHN synapses exhibit target-cell-specific short-term plasticity and recovery

Synapses can implement adaptation via short-term depression and the associated dynamics of recovery from depression.[32] The differences in adaptation and input specificity between LHN types suggested that plasticity from the same PN may differ for different target LHNs. To test this, we examined the voltage responses of LHN1 and LHN2 evoked by direct stimulation of DM1. We delivered ten 100-ms pulses of 100–300 pA depolarizing current at 5 Hz into DM1 via a patch pipette, evoking 7.2 ± 1.1 (mean ± SD) spikes per pulse (Figures 3A and 3B, bottom traces; STAR Methods). Simultaneous recordings from either LHN1 or LHN2 revealed responses that recapitulated odor stimulation: LHN1 maintained large depolarizations to each pulse whereas LHN2 responded strongly only to the first two pulses (Figures 3A and 3B, top traces).

This experimental configuration enabled us to measure unitary excitatory postsynaptic potentials (uEPSPs, the synaptic voltage response to individual spikes) evoked by DM1 spike trains. The volley of DM1 spikes during the first pulse (which always followed at least 8 s of quiescence to allow for synapses to recover) revealed a striking difference in short-term plasticity between synapses onto LHN1 and LHN2. The first DM1 spike evoked a large uEPSP in LHN1, but subsequent uEPSPs were smaller (Figure 3A, right). In contrast, the first DM1 spike evoked a very small uEPSP in LHN2, but subsequent uEPSPs were larger (Figure 3B, right). Across all recorded pairs, the first four uEPSPs (of the first current pulse) in LHN1 exhibited depression, whereas the first four uEPSPs in LHN2 exhibited facilitation (Figures 3C and 3D). Accordingly, quantal analysis (STAR Methods) predicted substantially higher initial release probability for synapses onto LHN1 than onto LHN2, with no change in quantal size (Figure 3E).

Over subsequent pulses, uEPSP amplitudes were smaller than those in the first pulse for both LHN1 and LHN2 (Figures 3C and 3D). This suggests that synaptic depression operates at both synapses and requires more than the 100-ms pause between pulses to fully recover. Within each pulse, in contrast, the first four uEPSP amplitudes decreased in LHN1 but increased in LHN2 (Figures 3C and 3D). This suggests that synaptic facilitation at the DM1-LHN2 synapse recovers more completely than depression during the brief pauses between pulses.

To better understand the dynamics of these synapses, we fit quantitative phenomenological models[33] of short-term plasticity to our uEPSP amplitude measurements (STAR Methods). Because the DM1-LHN1 synapse displayed no evidence of facilitation, we used a model with only depression (Figure 3F), which fit very well (Figure 3H, left). This model matched the intuition of a relatively slow recovery from depression, which builds up over repeated pulses until it stabilizes (Figure 3I). A model with both depression

and facilitation fit our data for the DM1-LHN2 synapse (Figures 3G and 3H). The parameters of this model also matched our intuition, with an even slower recovery from depression paired with fast recovery from facilitation (Figure 3I). This separation of timescales highlights the importance of facilitation for LHN2's transience: a rapid increase in DM1 spike rate facilitates the synapse before much depression accumulates, but slowly recovering depression soon "catches up" and overwhelms facilitation.

Presynaptic calcium in DM1 regulates odor-coding dynamics in LHN2

Short-term plasticity usually depends on presynaptic mechanisms,[34] with facilitation classically arising from accumulation of presynaptic calcium.[35] Accordingly, presynaptic dialysis with the slow calcium buffer EGTA selectively blocks facilitation without affecting depression.[6] If synaptic facilitation is at least partly responsible for transient responses in LHN2, then dialyzing DM1 with EGTA would selectively reduce LHN2 responses to the first current injection pulse (when facilitation of the DM1-LHN2 synapse dominates over depression). In contrast, EGTA should not affect LHN1 (because the DM1-LHN1 synapse exhibits no facilitation).

To test these predictions, we repeated the same experiments as above, except we included 1 mM EGTA in the DM1 patch pipette. (Note that this is frequently included in "standard" internal solution recipes for *Drosophila*; STAR Methods.) We first compared LHN responses to DM1 current pulses before and after dialysis. In recordings from LHN1 (Figure 4A), we observed no substantial changes to either net depolarization or spike rate per pulse (Figure 4B). Similarly, no changes over the same time window were observed when EGTA was omitted from the pipette (Figure 4C). In contrast, EGTA dialysis of DM1 reduced both the net depolarization and spike rate of LHN2 during the first current pulse (Figures 4D and 4E). These effects vanished when EGTA was omitted from the DM1 pipette (Figure 4F). Overall, the net effect of EGTA was significantly greater for LHN2 than for LHN1 (Figures 4G–4J).

Importantly, EGTA reduced the facilitation of uEPSP amplitudes in LHN2 over the first few spikes of the first current pulse (when facilitation is most evident; Figures 4K and 4L). However, it did not affect uEPSP amplitudes during the last 5 current pulses (Figure 4K). These dynamics are consistent with either a reduction in facilitation amplitude or an increase in facilitation recovery rate. Differences in calcium signaling at different presynaptic sites of the same PN axon therefore contribute to different forms of short-term plasticity, which leads to differences in transience between LHN types.

Interestingly, the presynaptic DM1 terminals that target LHN1 and LHN2 do not segregate according to their position within the DM1 axon arbor or within the lateral horn neuropil (Figure S6). This suggests that short-term plasticity is not determined by PN axon-branch-specific regulation or cell-extrinsic spatial gradients. Rather, it is likely determined by the identity of the postsynaptic neuron, akin to similar synapses in the hippocampus.[36]

Unc13B boosts initial LHN2 responses to rapid increases in odor intensity

Our results so far indicate that the DM1-LHN2 synapse contributes to the transience of LHN2 odor responses
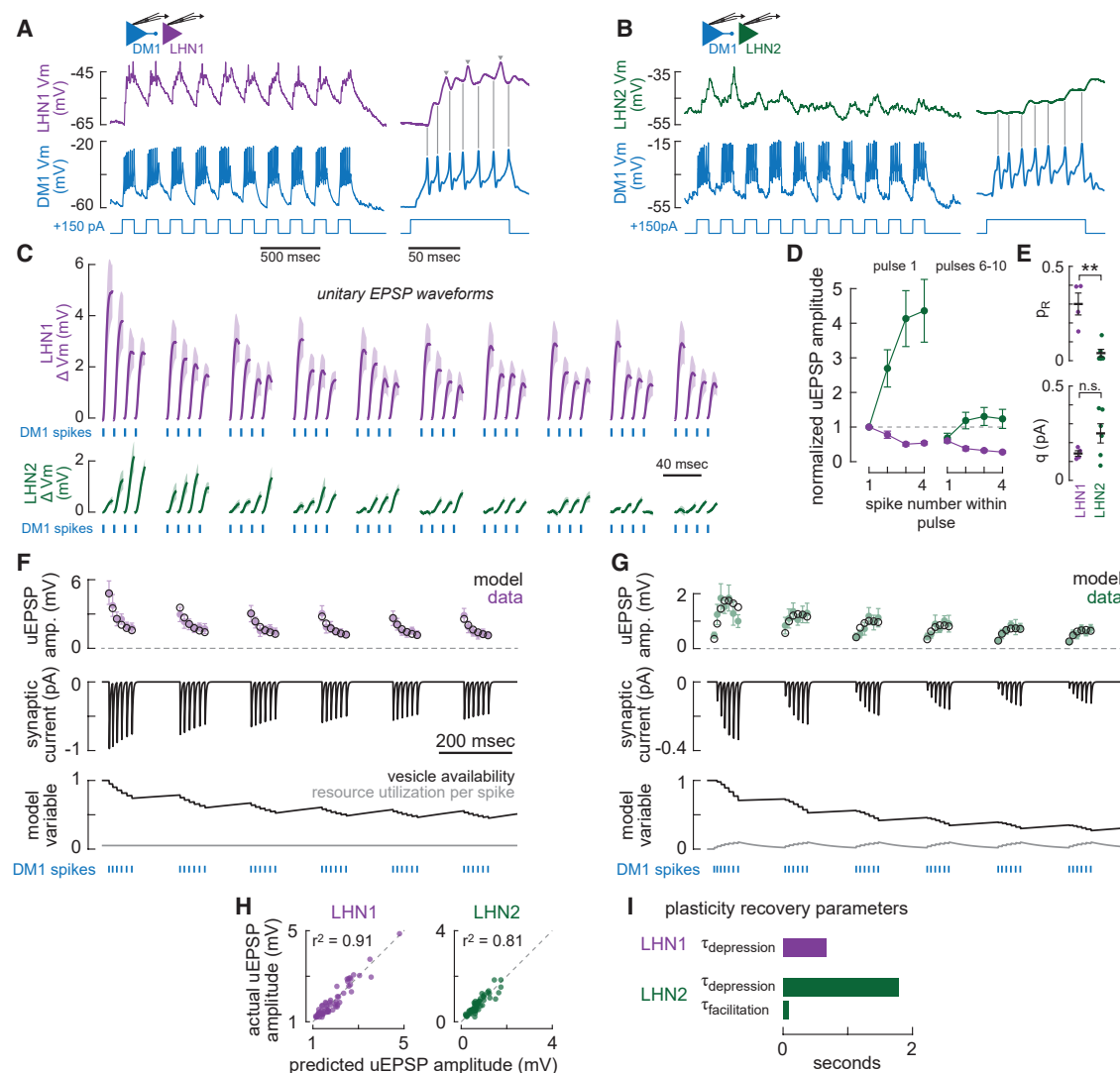
Figure 3. PN-LHN synapses exhibit target-cell-specific short-term plasticity and recovery

(A) Example paired recording from DM1 and LHN1 showing applied-current-evoked DM1 spikes (to mimic 5 Hz odor pulse responses) and corresponding postsynaptic responses in LHN1. Right: detail of the response to the first current pulse. Gray arrowheads denote LHN action potentials.

(B) Same as (A) but for DM1 and LHN2.

(C) Mean (±SEM) uEPSP waveforms measured in LHN1 (n = 4 pairs) or LHN2 (n = 6 pairs) for the first four DM1 spikes of each current pulse. Each uEPSP waveform is displayed on the same timescale, but each uEPSP is spaced uniformly for clarity. The gap between pulses is not to scale.

(D) Normalized uEPSP amplitude for DM1-LHN1 (purple) and DM1-LHN2 (green) synapses for the first four spikes of the first pulse and the first four spikes averaged over the last 5 pulses.

(E) Initial probability of release (top) and quantal content (bottom) for synapses from DM1 onto LHN1 and LHN2 estimated from paired recordings using quantal theory and inference of the number of release sites from the hemibrain connectome (STAR Methods). t test, **$p < 0.002$.

(F) Depression-only model (STAR Methods) of mean DM1-evoked uEPSP amplitudes in LHN1 (top). Model prediction of synaptic current (middle). Underlying model variables (bottom). Fraction of resource utilization per spike is constant in a model with only depression.

(G) Facilitation and depression model (STAR Methods) of mean DM1-evoked uEPSP amplitudes in LHN2 (top). Model prediction of synaptic current (middle). Underlying model variables (bottom). Fraction of resource utilization per spike changes due to facilitation.

(H) Models of each synapse type account for most of the variance in uEPSP amplitude.

(I) Fitted time constants of recovery from depression and facilitation in each model. Synapses onto LHN1 recover from depression faster than synapses onto LHN2. Synapses onto LHN2 recover from facilitation faster than they recover from depression.

See also Figure S6.

through a combination of short-term facilitation and slow recovery from depression. We next investigated the molecular mechanisms at the DM1-LHN2 synapse that contribute to adaptation.

EGTA-sensitive synaptic facilitation typically occurs when presynaptic calcium channels are relatively distantly coupled to calcium sensors.[6,37–39] This is because EGTA is too slow to affect closely coupled release sites, where calcium rapidly reaches
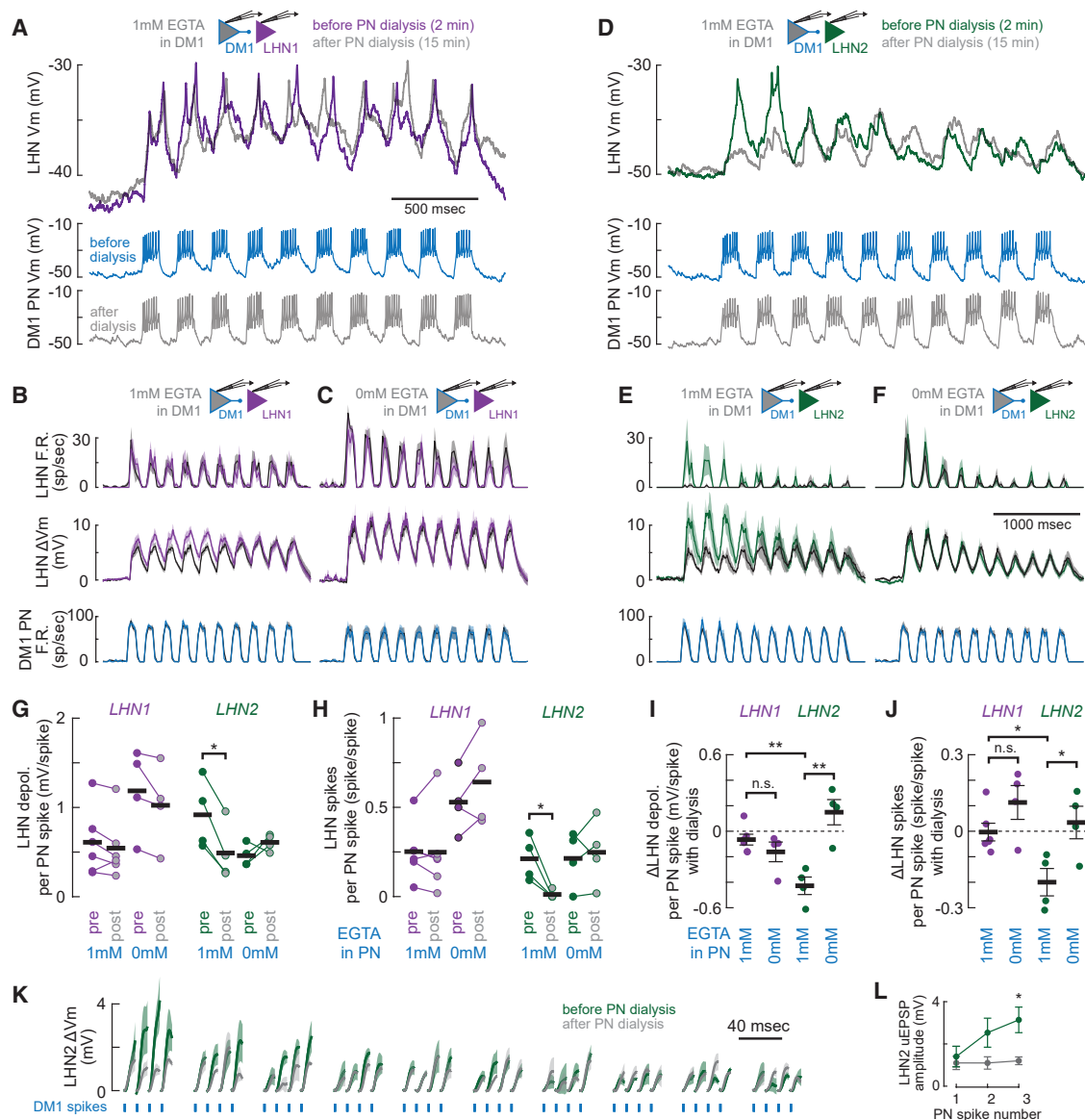
Figure 4. Presynaptic calcium in DM1 regulates odor-coding dynamics in LHN2

(A) Top: individual example traces of LHN1 activity before (purple) and after (gray) PN dialysis with 1 mM EGTA. Bottom: example traces of PN activity (simultaneously recorded with the LHN1 traces at top) before (blue) and after (gray) dialysis (evoked via current injection as in Figures 3A and 3B).

(B) Bottom: mean (±SEM) DM1 spike rates evoked by applied current before (blue) and after (gray) dialysis with 1 mM EGTA. Middle: mean (±SEM) LHN1 membrane potential before (purple) and after (gray) PN dialysis. Top: mean (±SEM) LHN1 spike rate before (purple) and after (gray) PN dialysis (n = 6 pairs).

(C) Same as (B) but without EGTA in the PN pipette (n = 4 pairs).

(D) Same as (A) but for LHN2.

(E) Same as (B) but for LHN2 (n = 3 pairs).

(F) Same as (C) but for LHN2 (n = 4 pairs).

(G) LHN1 depolarization per PN spike (during the first applied current pulse) did not change following PN dialysis with EGTA but LHN2 depolarization did (paired t test, p = 0.008). PN dialysis with internal saline lacking EGTA had no significant effect on LHN1 or LHN2 depolarization.

(H) LHN1 spikes per PN spike (during the first applied current pulse) did not change following PN dialysis with EGTA but LHN2 spikes did (paired t test, p = 0.03). PN dialysis with internal saline lacking EGTA had no significant effect on LHN1 or LHN2 spikes per PN spike.

(I) Dialysis with EGTA reduces the depolarization per PN spike for LHN2 more than without EGTA (t test, p = 0.003). There is no corresponding difference for LHN1 (t test, p = 0.27). The EGTA-induced reduction for LHN2 is larger than it is for LHN1 (t test, p = 0.001).

(J) Dialysis with EGTA reduces the number of LHN spikes per PN spike for LHN2 more than without EGTA (t test, p = 0.03). There is no corresponding difference for LHN1 (t test, p = 0.13). The EGTA-induced reduction for LHN2 is larger than it is for LHN1 (t test, p = 0.01).

(legend continued on next page)

the sensor.[37] Coupling distances are mediated, in part, by presynaptic Unc13 proteins, which also impact short-term plasticity.[40] In *Drosophila*, the Unc13B isoform specifically mediates long coupling distances, participates at facilitating synapses, and is present in the lateral horn.[41–43] Unc13B may therefore contribute to LHN2's initial responses to rapid increases in odor intensity.

To test this hypothesis, we reduced Unc13B expression in DM1 using RNAi (Figure 5A; STAR Methods). This manipulation reduced odor-evoked initial transient depolarizations in LHN2 but not LHN1 (Figures 5B and 5C), paralleling DM1 dialysis with EGTA. Importantly, it did not affect methyl acetate responses (which activate the DM4 PN) in LHN2, indicating that this manipulation is indeed selective for DM1 (Figures 5B and 5C).

We used a linear filter to model LHN2's voltage response (after adaptation to 5 Hz odor pulses) based on DM1 spike times (as in Figure 2A). We then used the same filter to predict the transient voltage response when odor pulses increased to 10 Hz (Figure 5D). The model significantly underpredicted these responses in control flies, consistent with a transient nonlinear boosting of DM1-LHN2 synaptic strength (Figures 5D and 5E; as expected from Figures 2A–2D). However, in flies with knockdown of Unc13B in DM1, a linear model was a good fit for the corresponding responses (Figures 5D and 5E). Thus, Unc13B in DM1 was necessary for the nonlinear boosting of LHN2 responses to rapid increases in odor intensity.

The effect of Unc13B knockdown on LHN2 voltage was large enough to impact spike rates. The transient increase in spike rate after increasing the odor pulse rate from 5 to 10 Hz was significantly smaller in Unc13B knockdown flies than in control flies, although steady-state spike rates were unchanged (Figures 5F and 5G). Accordingly, the adapted DM1-LHN2 input-output function became almost perfectly linear with knockdown of Unc13B (Figures 5H–5J). Comparing responses across multiple adapting and test stimulus frequencies revealed that reducing Unc13B expression impaired the fidelity with which LHN2 encoded positive changes in odor intensity (Figure 5K). These data show that presynaptic Unc13B boosts LHN2's initial transient responses without boosting sustained responses.

The Na$^+$/K$^+$ ATPase implements a cellular form of gain control in LHN1

LHN1 adapts by divisively adjusting its gain, reducing spike rates modestly enough that it still sustains responses to ongoing odor (Figures 1G and 1H). Because LHN1 cross-adapts across different PN inputs (Figure S5), gain control likely arises from a cell-intrinsic mechanism rather than from the synaptic dynamics of its PN inputs. In principle, this requires storing a cellular "memory" of recent activity with which to adjust responses to future synaptic inputs. How does LHN1 implement this?

Interestingly, LHN1 accumulates hyperpolarization after each odor pulse (when spaced far enough apart; Figures 6A and

6B). Hyperpolarization was also evident after pulses of current injection, suggesting a cellular origin because LHN1 has almost no feedback connections (Figures 6A–6C). These membrane potential dynamics resembled the electrogenic properties of the Na$^+$/K$^+$ ATPase (hereafter referred to simply as the sodium pump), which induces an outward current as it pumps sodium out of the cell.[44–46] High levels of activity can elevate intracellular sodium concentration enough to require seconds to tens of seconds of pump activity to reestablish equilibrium.[47] This stores a cellular memory of recent activity, which is "recalled" by the action of the sodium pump.[45] We hypothesized that this implements adaptive gain control in LHN1 (Figure 6D).

To test this, we genetically impaired the sodium pump selectively in LHN1 by overexpressing a dominant-negative version with a mutant alpha subunit ("dnATPase")[45,48] (Figure 6E). Expression of dnATPase caused inter-odor hyperpolarizations to grow more slowly over time (Figures 6A and 6B), allowing responses to the first few odor pulses to stay larger for longer (Figure 6A). Slowly accumulating outward currents should gradually counteract fast synaptic inward currents and is consistent with the narrowing of the linear filter with adaptation (Figures 2B and 2C).

We thus extended the linear filter model to include both a positive and negative lobe (until now, all such models had only a positive lobe) and used it to predict LHN1 voltage from DM1 spike rate. Adding the negative lobe allowed a single filter to accurately predict both adapted and unadapted voltage responses both for control LHNs and LHNs expressing dnATPase (Figure 6G). However, the filter for control LHNs had a significantly larger negative lobe than for dnATPase LHNs (Figures 6H and 6I), suggesting that the sodium pump contributes to the slow accumulation of outward current during repetitive stimulation.

If the sodium pump implements gain control in LHN1, then expressing dnATPase should attenuate the reduction in gain after adaptation. Indeed, dnATPase LHNs had larger transient elevations in spike rates than control LHNs when the odor pulse rate increased from 5 to 10 Hz (Figure 6J). It also eliminated the gain reduction of the DM1-LHN1 input-output function after adaptation to 5 Hz odor pulses (Figures 6K–6M) and disrupted divisive adaptation more broadly (Figures 6N and 6O). Thus, by taking advantage of the slow and activity-dependent dynamics of intracellular sodium, the sodium pump counteracts excitation to reduce gain on slow timescales but is not strong enough to completely suppress spiking to ongoing stimulation. This allows LHN1 to continuously respond to prolonged odors while modulating its sensitivity over time—a key feature of divisive adaptation that enables the neuron to reflect ongoing odor dynamics rather than just stimulus onset.

LHN1 and LHN2 make distinct contributions to odor-evoked upwind walking

The distinct dynamics of their physiological responses to odor suggest that LHN1 and LHN2 make distinct contributions to

---

(K) Mean (±SEM) uEPSP waveforms measured in LHN2 (n = 3 pairs) before and after DM1 dialysis with EGTA. Each uEPSP waveform is displayed on the same timescale but spaced uniformly for clarity. As in Figure 3C, the gap between pulses is not to scale.

(L) Mean (±SEM) uEPSP amplitude evoked by first three DM1 spikes before (green) and after (gray) DM1 dialysis with EGTA (n = 4 pairs). The facilitation observed before dialysis is abolished after dialysis (t test, *p = 0.021).

See also Figure S6.

Current Biology
Article

CellPress
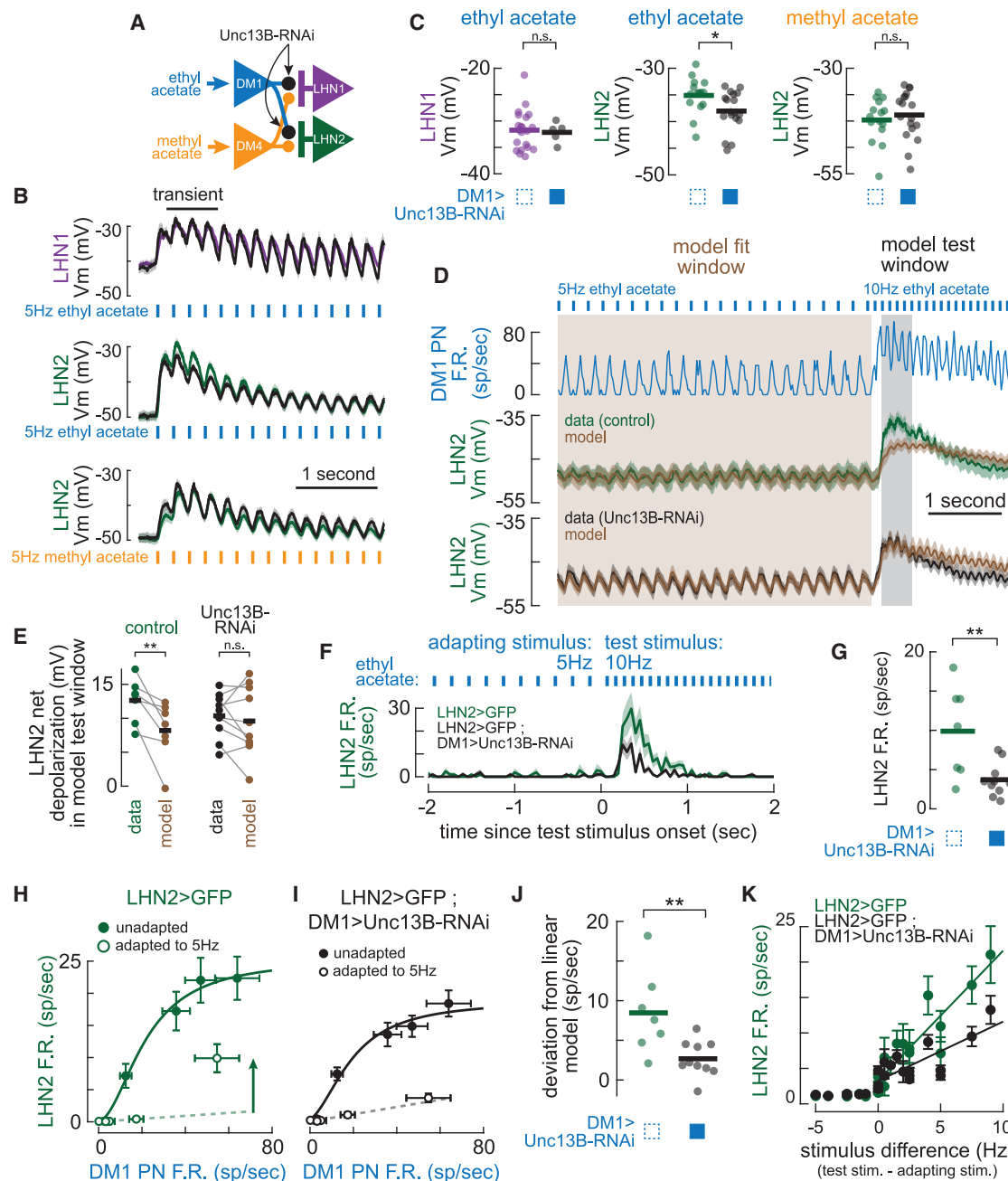
Figure 5. Unc13B boosts transient LHN2 responses to rapid increases in odor intensity

(A) Schematic of experimental manipulation reducing Unc13B expression in DM1 PN axon terminals (but not in DM4 PN axon terminals).

(B) Mean (shading denotes SEM) LHN1 voltage in response to ethyl acetate (top), LHN2 voltage in response to ethyl acetate (middle), and LHN2 voltage in response to methyl acetate (bottom). Purple and green traces are in control conditions (n = 21, 15, and 15, respectively); black traces are in flies with DM1 Unc13B knockdown (n = 5, 18, and 18, respectively). Bar at top denotes transient window used for quantification in (C).

(C) Average transient voltage (across "transient" time window denoted in B) for each recorded LHN in each of the three conditions in (B). Unc13B has no effect on ethyl acetate responses in LHN1 (left). Unc13B reduces the transient response in LHN2 (middle) t test, p = 0.025. Unc13B has no effect on methyl acetate responses in LHN2 (right).

(D) Average DM1 spike rate (top, n = 4), control LHN2 voltage (middle, n = 7), and LHN2 voltage with Unc13B knockdown in DM1 (bottom, n = 10) in response to ethyl acetate increasing from 5 to 10 Hz. Linear filter parameters are optimized to fit LHN voltages solely within the "model fit window." The filter is then used to predict responses to the entire stimulus. The "model test window" is used for the analysis in (E).

(E) At the increase in odor pulse frequency to 10 Hz, the linear model systematically underpredicts LHN2 voltage in control conditions (n = 7; t test, p = 0.015). The linear model does not systematically underpredict LHN2 voltage when Unc13B is knocked down in DM1 (n = 10; p = 0.50).

(legend continued on next page)

the dynamics of odor-guided behavior. LHN1 is known to have a context-specific behavioral role, which depends on odor concentration, learning, hunger, and locomotion modality (flight vs. walking).[21,49,50] Direct activation of LHN2 is known to drive modest attraction.[21] However, the roles of these two LHN types in behavioral responses to dynamic odor patterns is unknown.

We expressed the optogenetic channel CsChrimson in DM1 ORNs using Or42b-LexA[51] (Figure 7A) and delivered full-field light flashes to freely walking flies in a large wind tunnel (Figure 7B). Constant airflow provided a stable upwind direction to the flies and constant green light flooded the visual system, blunting visual responses to red light.[28,52,53] Flies were imaged from above and their walking trajectories were automatically extracted from videos (STAR Methods). Pulses of red light evoked time-locked increases in upwind velocity, which were not due to direct activation of the visual system (Figure S7A; STAR Methods). We identified split-Gal4 driver lines from published collections that expressed in either LHN1 (LH989-Gal4) or LHN2 (LH290-Gal4).[54] These lines are highly selective for each LHN type (with minimal off-target expression; Figure 7C) and were used to silence the synaptic output of each LHN type with the temperature-sensitive dynamin shibire[55] (STAR Methods).

To mimic the pulsed odor stimulation from our physiology experiments, we delivered pulses of red light starting at 5 Hz and then changed the frequency to either 10 or 2.5 Hz (Figure 7D). In parental control genotypes, flies maintained an elevated upwind walking velocity throughout 5 Hz stimulation. When the light intensity increased to 10 Hz, flies transiently surged upwind (Figure 7D, left traces). When the light intensity decreased to 2.5 Hz, flies maintained an elevated upwind velocity, although slightly slower than during 5 Hz stimulation (Figure 7D, right traces).

When we blocked synaptic output from LHN1, the high-intensity surge persisted, but low-intensity maintenance was lost (Figures 7D–7F). This corresponded to LHN1's sustained responses to ongoing 2.5 Hz stimulation. However, it did not correspond to LHN1's elevated responses to 10 Hz stimulation. This suggests that LHN1 has a nuanced role in guiding behavior that may be overshadowed by the activity of other LHN types when stimulus intensity is high. We also targeted LHN1 using a different split-Gal4 driver line (LH991-Gal4,[21] which has different but more substantial off-target expression than LH989-Gal4), but these experiments were inconclusive because of atypical walking patterns in the LH991-Gal4/+ parental controls (Figure S7). Previously, it has been shown that silencing LH989-expressing neurons impairs innate attraction to odors that strongly drive the PNs that feed into LHN1 but does not impair attraction to odors that more weakly drive them.[49,56]

This suggests that it is specifically the silencing of LHN1—and not the ventral nerve cord neurons—that causes the behavioral deficits we observe when expressing shibire under LH989-Gal4 control. However, we cannot completely rule out any contribution from these off-target neurons (Figure S7).

When we blocked synaptic output from LHN2, the high-intensity surge was lost, but low-intensity maintenance was preserved (Figures 7D–7F). These effects corresponded to LHN2's transient spiking responses to increases in stimulus intensity. Nearly identical effects were observed when we targeted LHN2 using a different split-Gal4 driver line (SS01372-Gal4, which has different off-target expression; Figure S7).[57] Thus, the divergent processing that begins with subcellular synaptic specializations in PNs creates specialized neuronal representations that can guide specific dynamic components of behavior.

DISCUSSION

Different implementations for different types of adaptation
Adaptation can arise from a range of mechanisms but always involves some form of slow, activity-dependent negative feedback.[58] The negative feedback responsible for LHN1 adaptation is implemented, at least in part, by the cell-intrinsic Na$^+$/K$^+$ ATPase, meaning that it depends on LHN1's own cellular activity (i.e., spiking). The strong DM1-LHN1 synapse ensures that even modest DM1 activity can drive LHN1 above its spike threshold. Adaptation reduces the gain of LHN1's tuning curve but cannot prevent spiking altogether, meaning that LHN1 remains within a suprathreshold regime, ensuring sustained spiking. This configuration leads to LHN1 encoding the ratio of the current stimulus intensity to the prior stimulus intensity, regardless of which PN inputs are active.

In contrast, the negative feedback responsible for LHN2 adaptation is implemented by the especially slow recovery from depression at PN presynapses, meaning that adaptation does not depend on LHN2's own cellular activity. When DM1 spike rates rapidly increase, the DM1-LHN2 synapse facilitates to enable strong synaptic transmission, likely dependent on Unc13B. But during constant DM1 activity, the accumulating effects of depression overwhelm facilitation, reducing transmission to a level insufficient to drive LHN2 above its spike threshold. Therefore, adaptation introduces an expansive nonlinearity to LHN2's tuning curve, simply by enabling synaptic depolarizations to span sub- and suprathreshold regimes, yielding only transient responses to a sustained odor. This

(F) Mean (±SEM) PSTHs of LHN2 responses to ethyl acetate pulse frequency increasing from 5 to 10 Hz. In control conditions (green, $n = 7$), transient LHN2 activity is larger than with DM1 Unc13B knockdown (black, $n = 10$). Only the last 2 s of the 20 s adapting 5 Hz stimulus is shown.

(G) The increase from 5 to 10 Hz evokes a larger transient firing rate (average over 1 s of 10 Hz stimulation) for control LHN2 than for LHN2 with Unc13B knocked down in DM1 ($p = 0.0068$).

(H) Input-output functions relating mean (±SEM) DM1 spike rates ($n = 4$–8) to mean (±SEM) LHN2 spike rates, without adaptation (solid circles, $n = 10$–12) and after adaptation to 5 Hz ethyl acetate (open circles, $n = 7$). The adapted responses for odor pulse rates at and below the adapting frequency were fit with a linear model (dashed line). Arrow denotes the deviation of the 10 Hz response from the linear model prediction. Data are repeated from Figure 2H for ease of comparison to (I).

(I) Input-output functions relating mean (±SEM) DM1 spikes rates to mean (±SEM) LHN2 spike rates, as in (G), but with Unc13B knockdown in DM1 ($n = 10$–18 LHN2 recordings).

(J) Unc13B knockdown reduces the deviation from the linear model of the adapted response (dashed lines in H and I; t test, $p = 0.0071$).

(K) Mean (±SEM) LHN2 spike rates plotted as a function of stimulus difference (test stimulus frequency minus adapting frequency) for control conditions and with Unc13B knockdown in DM1. Unc13B knockdown significantly reduces the slope for increases in stimulus frequency (ANCOVA interaction, $p = 0.0002$).

Current Biology
Article

CellPress
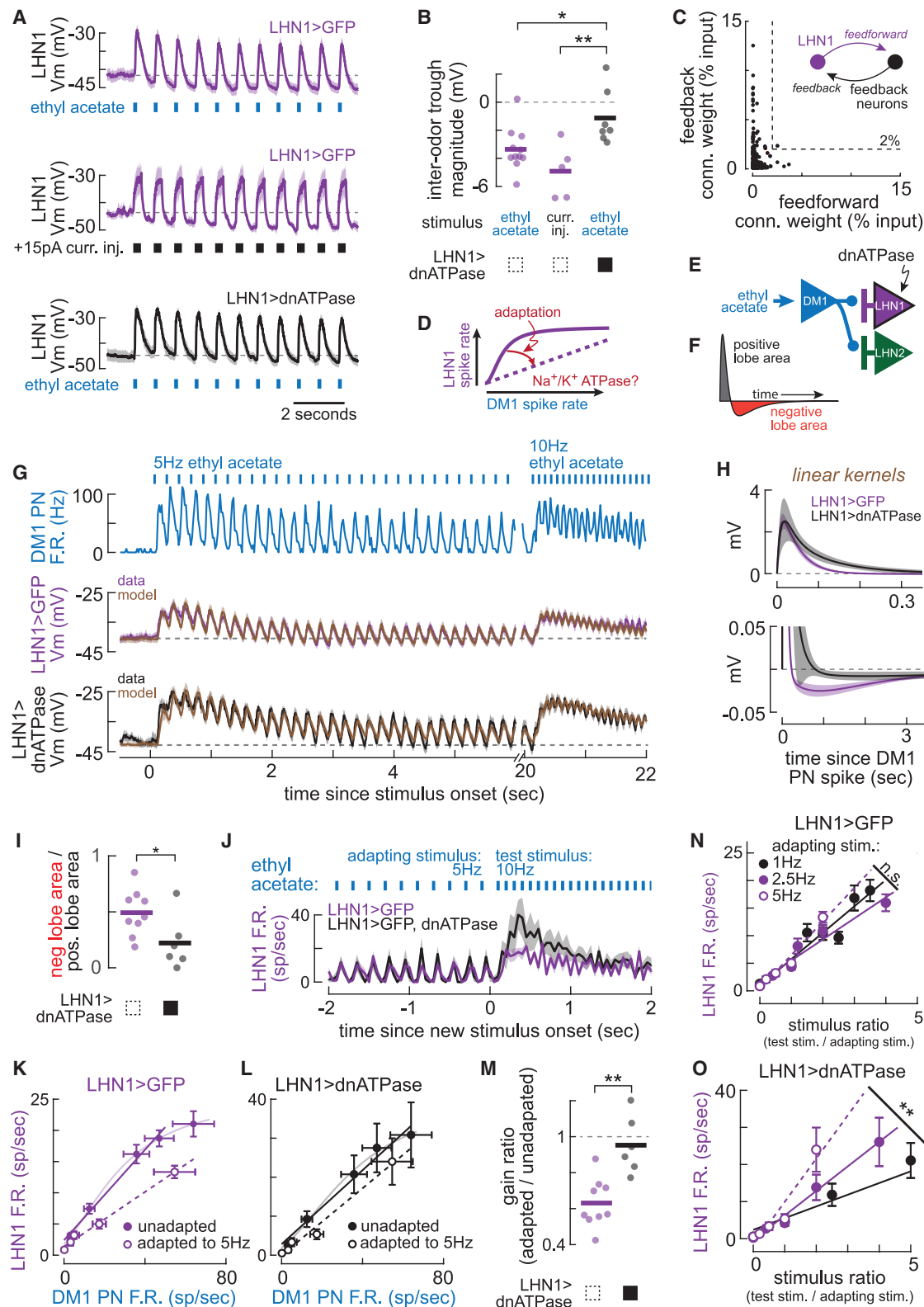
Figure 6. The Na$^+$/K$^+$ ATPase implements a cellular form of gain control in LHN1

(A) Mean (±SEM) voltage in LHN1 in response to 1.25 Hz odor pulse stimulation (top; $n = 11$) and 1.25 Hz current injection pulses (middle; $n = 5$). Bottom, LHN1 voltage in response to 1.25 Hz odor pulse stimulation in LHN1>dnATPase flies ($n = 7$).

configuration leads to LHN2 encoding the difference between the current stimulus intensity and the prior stimulus intensity but in an input-specific manner. Adaptation thus impacts the dynamics of LHN1 and LHN2 in different ways: it attenuates LHN1's spiking responses to changes in stimulus intensity and identity but accentuates LHN2's responses to them.

Origination of temporal diversity in central circuits

In other sensory systems, such as somatosensation, different dynamic representations originate immediately in different peripheral receptor types.[59] Why does the olfactory system postpone temporal diversification? One possibility is the need to detect weak and noisy signals, which benefits from averaging the activity of many ORNs expressing the same receptor.[29,60–62] Splitting each ORN population into transient and sustained subtypes would yield smaller populations of each, diminishing the benefits of averaging (assuming constraints on the total number of ORNs). Diversifying after averaging thus allows for maximal noise reduction. A similar organization exists in vision, where multiple photoreceptors converge onto bipolar cells, which then generate diverse temporal representations.[4] Originating temporal diversity centrally may thus be a particularly useful strategy when very weak sensory signals are important.

Creating temporal diversity through synaptic specializations provides at least two additional advantages. First, it is compact because it does not require interposed neurons to provide synaptic inhibition, so computation can be performed with fewer neurons. Second, it reduces redundancy as early as possible by suppressing unnecessary synaptic transmission, which reduces metabolic costs.[63,64] Interestingly, specific synaptic interactions may also underlie the generation of temporally diverse odor representations in different PNs.[65] This strategy may thus be widely used to conserve energy and to allow interposed neurons to perform other functions, such as implementing comparisons across sensory space.[3,66,67]

Target-neuron-specific synaptic dynamics and behavioral specialization

Target-neuron-specific short-term plasticity (and corresponding recovery from plasticity) in the brain is likely a ubiquitous phenomenon,[5–10,68] but its role in generating circuit-level segregation of computation and behavior has not been clear. By studying this motif in the central brain of *Drosophila*, we discovered that it serves to separate transient and sustained dynamics from a single neuron. Moreover, the resulting parallel pathways lead to independent regulation of corresponding components of the behavioral response to fictive odor patterns, demonstrating distinct functional roles for these synaptic dynamics.

The functions of higher-order olfactory neurons are traditionally characterized as either attractive or aversive, linking specific chemical combinations to valence.[21,69,70] The separation of transient and sustained activity into parallel channels may indicate that temporal dynamics may further subdivide attractive and aversive neurons. Higher-order olfactory neurons may thus link specific chemotemporal combinations to specific instinctive behavioral programs. The 10-fold expansion of cell types in the lateral horn (~50 uniglomerular PN types target ~500 LHN types[12]) seemingly provides an ample anatomical basis for this kind of specialization. Correspondingly, broad chemotemporal diversity has been reported across LHNs in both fly[3,15] and locust.[71]

Building blocks of dynamic network function

The divergent circuitry in the lateral horn operates by combining simple building blocks: short-term depression and facilitation, spike threshold, and a slow activity-dependent outward current. These are implemented by molecular mechanisms, including Unc13B and the Na$^+$/K$^+$ ATPase, that are conserved across taxa. These molecules may therefore provide broad insights into the dynamic function of networks currently only identified by static connectivity maps.

Expression of Unc13B is not uniform throughout the brain, so its presence at any given synapse may predict dynamics.[42] Mapping

(B) Net change in voltage between baseline (prior to stimulation) and the interstimulus intervals for each condition in (A). Expression of dnATPase in LHN1 decreases inter-odor hyperpolarization compared with control LHNs (t tests, *p = 0.016; **p = 0.007).

(C) There is minimal di-synaptic feedback onto LHN1 in the hemibrain connectome. Each point denotes one neuron receiving input from, or providing output to, LHN1. Only one neuron (of type SMP443) receives more than 2% of its input from LHN1 while also providing more than 2% of LHN1's input.

(D) Schematic of hypothesis tested here, that the Na$^+$/K$^+$ ATPase underlies adaptive gain control in LHN1.

(E) Schematic of experimental manipulation.

(F) Schematic of biphasic filter shape used to model LHN1 voltages from DM1 spike times in (G).

(G) Average DM1 spike rate (top, n = 4), control LHN1 voltages (middle, n = 9), and LHN1>dnATPase voltages (bottom, n = 6) in response to ethyl acetate increasing from 5 to 10 Hz. Biphasic linear filters (H) accurately fit the entire voltage response in both control and dnATPase conditions (superposed brown traces), based on the DM1 spike pattern.

(H) Mean (±SEM) best-fit filters for control and dnATPase conditions. Top and bottom panels plot the same data but on different time and voltage scales.

(I) The ratio of negative lobe area to positive lobe area is larger in control LHNs than in LHNs expressing dnATPase (t test, *p = 0.036).

(J) Mean (±SEM) PSTHs of control LHN1 activity (purple, n = 8) and LHN1>dnATPase activity (black, n = 6) in response to ethyl acetate pulse frequency increasing from 5 to 10 Hz. Only the last 2 s of the 20-s 5 Hz stimulation are shown. The spike rate during the first 1-s window of the 10 Hz stimulus is higher for control LHNs than for LHNs expressing dnATPase (t test, *p = 0.049).

(K) Input-output functions relating mean (±SEM) DM1 spike rates (n = 4–8) to mean (±SEM) LHN1 spike rates, without adaptation (solid circles, n = 5–16) and adapted to 5 Hz ethyl acetate (open circles, n = 9). Error bars denote SEM. The linear regime of the unadapted (solid purple line) and adapted (dashed line) responses are fit with linear models. The full nonlinear model is shown in the pale purple line for comparison. Data are repeated from Figure 2G for ease of comparison to (L).

(L) Input-output functions relating DM1 spikes rates to LHN1 spike rates, as in (K), but with dnATPase expression in LHN1 (n = 6 LHN recordings).

(M) dnATPase expression in LHN1 reduces the gain ratio (adapted/unadapted) of the DM1-LHN1 input-output function (**t test, p = 0.001).

(N) Mean (±SEM) spike rates in control LHN1 as a function of stimulus ratio (test stimulus frequency divided by adapting stimulus frequency). Linear fits for each adapting frequency have statistically indistinguishable slopes (ANCOVA interaction, p = 0.71).

(O) Mean (±SEM) spike rates in LHN1>dnATPase recordings as a function of stimulus ratio (test stimulus frequency divided by adapting stimulus frequency). Linear fits for each adapting frequency have different slopes (**ANCOVA interaction, p = 0.0004).

Current Biology
Article

🖉 CellPress
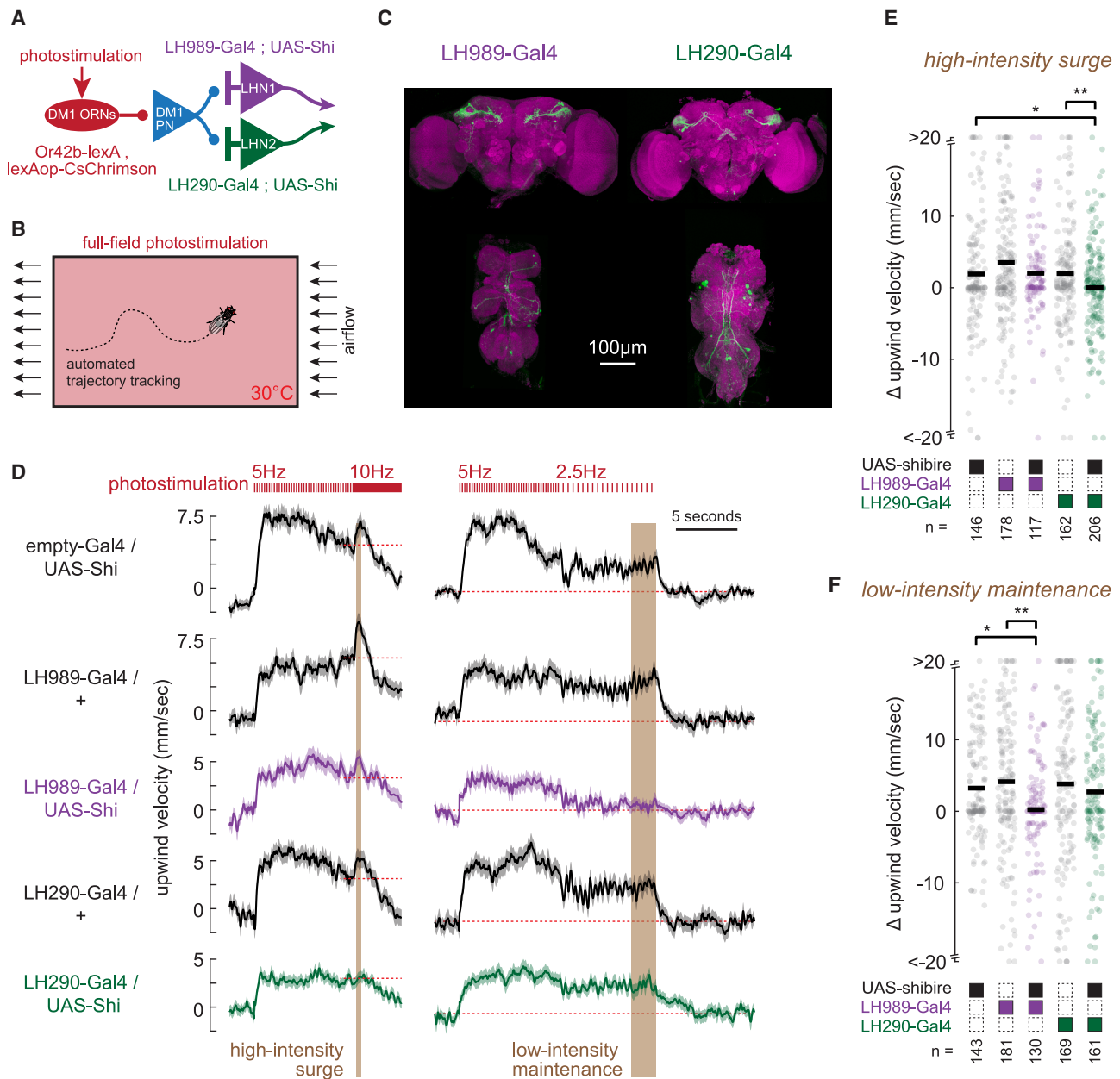
Figure 7. LHN2 contributes to transient upwind surge behavior

(A) Schematic of genetic manipulation. The DM1 PN is activated via photostimulation of its cognate ORNs. The synaptic output of each LHN type is silenced using selective Gal4 drivers.

(B) Schematic of the behavioral arena.

(C) Expression patterns of the Gal4 lines used to silence each LHN type.

(D) Mean (±SEM) upwind velocity traces of flies in each genotype to 5–10 Hz photostimulation and 5–2.5 Hz poststimulation patterns. Data for genotypes that silence LHN1 and LHN2 are displayed in purple and green, respectively. Parental control genotypes are displayed in black. Red dashed lines denote the mean velocity just prior to the increase to 10 Hz (left) or the baseline velocity in the absence of stimulation (right). Gray background shading denotes time windows for analysis of the high-intensity surge and low-intensity maintenance analyzed in (E) and (F).

(E) Summary of the magnitude of the high-intensity surge for all flies in each genotype. Each point denotes one fly trajectory, sample sizes specified at the bottom denote number of trajectories. t tests, *$p < 0.02$; **$p < 0.01$.

(F) Same as (E) but for the magnitude of the low-intensity maintenance. t tests, *$p < 0.003$; **$p < 0.001$.

See also Figure S7.

Unc13B expression with synaptic resolution could, in principle, constrain the short-term dynamics of every synapse in the brain. In contrast, the Na⁺/K⁺ ATPase exists in every neuron and its impact on activity likely depends on the specific dynamics of synaptic inputs. An important goal for the future is therefore to define the principles of how these and other dynamic building blocks interface with each other. Incorporating these principles into connectome-constrained network models should lead to better predictions of their computations and behavioral consequences.[72]

Limitations of the study

To identify the mechanisms of divergent information processing from one PN to multiple LHN types, we necessarily focused on simplified stimuli. The difference in cross-adaptation between LHN1 and LHN2 (Figure S4) indicates that odors that elicit more complex spatiotemporal glomerular activation patterns may yield further divergence in response dynamics. We also focused on just two of the ~500 LHN types.[12] Further studies will be necessary to determine whether the broader LHN population separates distinctly into transient and sustained types or whether other dynamic response patterns are prominent, such as spiking responses evoked by the cessation of odor.

RESOURCE AVAILABILITY

Lead contact
Further information and requests for resources and reagents should be directed to, and will be fulfilled by, the lead contact, James M. Jeanne (james.jeanne@yale.edu).

Materials availability
This study did not generate new unique reagents.

Data and code availability
- Electrophysiology and imaging data will be deposited and publicly available as of the date of publication. Accession numbers are listed in the key resources table.
- All original code has been deposited at Zenodo and is publicly available as of the date of publication. DOIs are listed in the key resources table.
- Any additional information required to reanalyze the data reported in this paper is available from the lead contact upon request.

AUTHOR CONTRIBUTIONS

H.S.K. and J.M.J. conceptualized the study. H.S.K. discovered the distinct dynamics between LHN1 and LHN2 and conducted the voltage imaging experiments. J.M.J. conducted electrophysiology experiments. H.S.K. and J.M.J. analyzed all physiology and imaging data. G.M.S. conducted behavior experiments. G.M.S., T.E., and J.M.J. analyzed behavior data. G.S. performed genetic crosses to generate experimental flies and performed confocal imaging. H.S.K. and J.M.J. wrote the paper with input from all authors.

DECLARATION OF INTERESTS

The authors declare no competing interests.

STAR★METHODS

Detailed methods are provided in the online version of this paper and include the following:

- KEY RESOURCES TABLE
- EXPERIMENTAL MODEL AND STUDY PARTICIPANT DETAILS
- METHOD DETAILS
  - Fly preparation for imaging and electrophysiology
  - Voltage Imaging
  - Electrophysiology
  - Freely moving walking behavior
  - Odor delivery and stimulus design
  - Immunohistochemistry and imaging
- QUANTIFICATION AND STATISTICAL ANALYSIS
  - Connectome analysis
  - Spike identification, analysis of spike rates, and analysis of membrane voltages
  - Curve fitting to odor tuning curves and cellular input-output functions
  - Behavior analysis

SUPPLEMENTAL INFORMATION

Supplemental information can be found online at https://doi.org/10.1016/j.cub.2025.05.051.

REFERENCES

1. Luo, L. (2021). Architectures of neuronal circuits. Science *373*, eabg7285. https://doi.org/10.1126/science.abg7285.

2. Igarashi, K.M., Ieki, N., An, M., Yamaguchi, Y., Nagayama, S., Kobayakawa, K., Kobayakawa, R., Tanifuji, M., Sakano, H., Chen, W.R., et al. (2012). Parallel mitral and tufted cell pathways route distinct odor information to different targets in the olfactory cortex. J. Neurosci. *32*, 7970–7985. https://doi.org/10.1523/JNEUROSCI.0154-12.2012.

3. Taisz, I., Donà, E., Münch, D., Bailey, S.N., Morris, B.J., Meechan, K.I., Stevens, K.M., Varela-Martínez, I., Gkantia, M., Schlegel, P., et al. (2023). Generating parallel representations of position and identity in the olfactory system. Cell *186*, 2556–2573.e22. https://doi.org/10.1016/j.cell.2023.04.038.

4. Demb, J.B., and Singer, J.H. (2015). Functional circuitry of the retina. Annu. Rev. Vis. Sci. *1*, 263–289. https://doi.org/10.1146/annurev-vision-082114-035334.

5. Reyes, A., Lujan, R., Rozov, A., Burnashev, N., Somogyi, P., and Sakmann, B. (1998). Target-cell-specific facilitation and depression in neocortical circuits. Nat. Neurosci. *1*, 279–285. https://doi.org/10.1038/1092.

6. Rozov, A., Burnashev, N., Sakmann, B., and Neher, E. (2001). Transmitter release modulation by intracellular Ca2+ buffers in facilitating and depressing nerve terminals of pyramidal cells in layer 2/3 of the rat neocortex indicates a target cell-specific difference in presynaptic calcium dynamics. J. Physiol. *531*, 807–826. https://doi.org/10.1111/j.1469-7793.2001.0807h.x.

Current Biology
Article

CellPress

7. Scanziani, M., Gähwiler, B.H., and Charpak, S. (1998). Target cell-specific modulation of transmitter release at terminals from a single axon. Proc. Natl. Acad. Sci. USA *95*, 12004–12009. https://doi.org/10.1073/pnas.95.20.12004.

8. Markram, H., Wang, Y., and Tsodyks, M. (1998). Differential signaling via the same axon of neocortical pyramidal neurons. Proc. Natl. Acad. Sci. USA *95*, 5323–5328. https://doi.org/10.1073/pnas.95.9.5323.

9. English, D.F., McKenzie, S., Evans, T., Kim, K., Yoon, E., and Buzsáki, G. (2017). Pyramidal cell-interneuron circuit architecture and dynamics in hippocampal networks. Neuron *96*, 505–520.e7. https://doi.org/10.1016/j.neuron.2017.09.033.

10. Davis, G.W., and Murphey, R.K. (1993). A role for postsynaptic neurons in determining presynaptic release properties in the cricket CNS: evidence for retrograde control of facilitation. J. Neurosci. *13*, 3827–3838. https://doi.org/10.1523/JNEUROSCI.13-09-03827.1993.

11. Pottackal, J., Singer, J.H., and Demb, J.B. (2021). Computational and molecular properties of starburst amacrine cell synapses differ with postsynaptic cell type. Front. Cell. Neurosci. *15*, 660773. https://doi.org/10.3389/fncel.2021.660773.

12. Schlegel, P., Bates, A.S., Stürner, T., Jagannathan, S.R., Drummond, N., Hsu, J., Serratosa Capdevila, L., Javier, A., Marin, E.C., Barth-Maron, A., et al. (2021). Information flow, cell types and stereotypy in a full olfactory connectome. eLife *10*, e66018. https://doi.org/10.7554/eLife.66018.

13. Fişek, M., and Wilson, R.I. (2014). Stereotyped connectivity and computations in higher-order olfactory neurons. Nat. Neurosci. *17*, 280–288. https://doi.org/10.1038/nn.3613.

14. Jeanne, J.M., Fişek, M., and Wilson, R.I. (2018). The organization of projections from olfactory glomeruli onto higher-order neurons. Neuron *98*, 1198–1213.e6. https://doi.org/10.1016/j.neuron.2018.05.011.

15. Frechter, S., Bates, A.S., Tootoonian, S., Dolan, M.J., Manton, J., Jamasb, A.R., Kohl, J., Bock, D., and Jefferis, G. (2019). Functional and anatomical specificity in a higher olfactory centre. eLife *8*, e44590. https://doi.org/10.7554/eLife.44590.

16. Nagel, K.I., Hong, E.J., and Wilson, R.I. (2015). Synaptic and circuit mechanisms promoting broadband transmission of olfactory stimulus dynamics. Nat. Neurosci. *18*, 56–65. https://doi.org/10.1038/nn.3895.

17. Wilson, R.I. (2013). Early olfactory processing in Drosophila: mechanisms and principles. Annu. Rev. Neurosci. *36*, 217–241. https://doi.org/10.1146/annurev-neuro-062111-150533.

18. Bates, A.S., Schlegel, P., Roberts, R.J.V., Drummond, N., Tamimi, I.F.M., Turnbull, R., Zhao, X., Marin, E.C., Popovici, P.D., Dhawan, S., et al. (2020). Complete connectomic reconstruction of olfactory projection neurons in the fly brain. Curr. Biol. *30*, 3183–3199.e3186. https://doi.org/10.1101/2020.01.19.911453.

19. Ruta, V., Datta, S.R., Vasconcelos, M.L., Freeland, J., Looger, L.L., and Axel, R. (2010). A dimorphic pheromone circuit in Drosophila from sensory input to descending output. Nature *468*, 686–690. https://doi.org/10.1038/nature09554.

20. Kohl, J., Ostrovsky, A.D., Frechter, S., and Jefferis, G.S.X.E. (2013). A bidirectional circuit switch reroutes pheromone signals in male and female brains. Cell *155*, 1610–1623. https://doi.org/10.1016/j.cell.2013.11.025.

21. Dolan, M.J., Frechter, S., Bates, A.S., Dan, C., Huoviala, P., Roberts, R.J., Schlegel, P., Dhawan, S., Tabano, R., Dionne, H., et al. (2019). Neurogenetic dissection of the Drosophila lateral horn reveals major outputs, diverse behavioural functions, and interactions with the mushroom body. eLife *8*, e43079. https://doi.org/10.7554/eLife.43079.

22. Matheson, A.M.M., Lanz, A.J., Medina, A.M., Licata, A.M., Currier, T.A., Syed, M.H., and Nagel, K.I. (2022). A neural circuit for wind-guided olfactory navigation. Nat. Commun. *13*, 4613. https://doi.org/10.1038/s41467-022-32247-7.

23. Semmelhack, J.L., and Wang, J.W. (2009). Select Drosophila glomeruli mediate innate olfactory attraction and aversion. Nature *459*, 218–223. https://doi.org/10.1038/nature07983.

24. Bell, J.S., and Wilson, R.I. (2016). Behavior reveals selective summation and max pooling among olfactory processing channels. Neuron *91*, 425–438. https://doi.org/10.1016/j.neuron.2016.06.011.

25. Tanaka, N.K., Endo, K., and Ito, K. (2012). Organization of antennal lobe-associated neurons in adult Drosophila melanogaster brain. J. Comp. Neurol. *520*, 4067–4130. https://doi.org/10.1002/cne.23142.

26. Olsen, S.R., Bhandawat, V., and Wilson, R.I. (2010). Divisive normalization in olfactory population codes. Neuron *66*, 287–299. https://doi.org/10.1016/j.neuron.2010.04.009.

27. Álvarez-Salvado, E., Licata, A.M., Connor, E.G., McHugh, M.K., King, B.M., Stavropoulos, N., Victor, J.D., Crimaldi, J.P., and Nagel, K.I. (2018). Elementary sensory-motor transformations underlying olfactory navigation in walking fruit-flies. eLife *7*, e37815. https://doi.org/10.7554/eLife.37815.

28. Jayaram, V., Sehdev, A., Kadakia, N., Brown, E.A., and Emonet, T. (2023). Temporal novelty detection and multiple timescale integration drive Drosophila orientation dynamics in temporally diverse olfactory environments. PLoS Comput. Biol. *19*, e1010606. https://doi.org/10.1371/journal.pcbi.1010606.

29. Jeanne, J.M., and Wilson, R.I. (2015). Convergence, divergence, and reconvergence in a feedforward network improves neural speed and accuracy. Neuron *88*, 1014–1026. https://doi.org/10.1016/j.neuron.2015.10.018.

30. Azouz, R., and Gray, C.M. (2000). Dynamic spike threshold reveals a mechanism for synaptic coincidence detection in cortical neurons in vivo. Proc. Natl. Acad. Sci. USA *97*, 8110–8115. https://doi.org/10.1073/pnas.130200797.

31. Weber, A.I., Krishnamurthy, K., and Fairhall, A.L. (2019). Coding principles in adaptation. Annu. Rev. Vis. Sci. *5*, 427–449. https://doi.org/10.1146/annurev-vision-091718-014818.

32. Chung, S., Li, X., and Nelson, S.B. (2002). Short-term depression at thalamocortical synapses contributes to rapid adaptation of cortical sensory responses in vivo. Neuron *34*, 437–446. https://doi.org/10.1016/s0896-6273(02)00659-1.

33. Tsodyks, M., Pawelzik, K., and Markram, H. (1998). Neural networks with dynamic synapses. Neural Comput. *10*, 821–835. https://doi.org/10.1162/089976698300017502.

34. Regehr, W.G. (2012). Short-term presynaptic plasticity. Cold Spring Harb. Perspect. Biol. *4*, a005702. https://doi.org/10.1101/cshperspect.a005702.

35. Jackman, S.L., and Regehr, W.G. (2017). The mechanisms and functions of synaptic facilitation. Neuron *94*, 447–464. https://doi.org/10.1016/j.neuron.2017.02.047.

36. Sylwestrak, E.L., and Ghosh, A. (2012). Elfn1 regulates target-specific release probability at CA1-interneuron synapses. Science *338*, 536–540. https://doi.org/10.1126/science.1222482.

37. Eggermann, E., Bucurenciu, I., Goswami, S.P., and Jonas, P. (2011). Nanodomain coupling between Ca(2)(+) channels and sensors of exocytosis at fast mammalian synapses. Nat. Rev. Neurosci. *13*, 7–21. https://doi.org/10.1038/nrn3125.

38. Rebola, N., Reva, M., Kirizs, T., Szoboszlay, M., Lőrincz, A., Moneron, G., Nusser, Z., and DiGregorio, D.A. (2019). Distinct nanoscale calcium channel and synaptic vesicle topographies contribute to the diversity of synaptic function. Neuron *104*, 693–710.e9. https://doi.org/10.1016/j.neuron.2019.08.014.

39. Vyleta, N.P., and Jonas, P. (2014). Loose coupling between Ca2+ channels and release sensors at a plastic hippocampal synapse. Science *343*, 665–670. https://doi.org/10.1126/science.1244811.

40. Dittman, J.S. (2019). Unc13: a multifunctional synaptic marvel. Curr. Opin. Neurobiol. *57*, 17–25. https://doi.org/10.1016/j.conb.2018.12.011.

41. Böhme, M.A., Beis, C., Reddy-Alla, S., Reynolds, E., Mampell, M.M., Grasskamp, A.T., Lützkendorf, J., Bergeron, D.D., Driller, J.H., Babikir, H., et al. (2016). Active zone scaffolds differentially accumulate Unc13 isoforms to tune Ca(2)+ channel-vesicle coupling. Nat. Neurosci. *19*, 1311–1320. https://doi.org/10.1038/nn.4364.

42. Fulterer, A., Andlauer, T.F.M., Ender, A., Maglione, M., Eyring, K., Woitkuhn, J., Lehmann, M., Matkovic-Rachid, T., Geiger, J.R.P., Walter, A.M., et al. (2018). Active zone scaffold protein ratios tune functional diversity across brain synapses. Cell Rep. 23, 1259–1274. https://doi.org/10.1016/j.celrep.2018.03.126.

43. Pooryasin, A., Maglione, M., Schubert, M., Matkovic-Rachid, T., Hasheminasab, S.M., Pech, U., Fiala, A., Mielke, T., and Sigrist, S.J. (2021). Unc13A and Unc13B contribute to the decoding of distinct sensory information in Drosophila. Nat. Commun. 12, 1932. https://doi.org/10.1038/s41467-021-22180-6.

44. Catarsi, S., Scuri, R., and Brunelli, M. (1993). Cyclic AMP mediates inhibition of the Na(+)-K+ electrogenic pump by serotonin in tactile sensory neurones of the leech. J. Physiol. 462, 229–242. https://doi.org/10.1113/jphysiol.1993.sp019552.

45. Pulver, S.R., and Griffith, L.C. (2010). Spike integration and cellular memory in a rhythmic network from Na+/K+ pump current dynamics. Nat. Neurosci. 13, 53–59. https://doi.org/10.1038/nn.2444.

46. Gulledge, A.T., Dasari, S., Onoue, K., Stephens, E.K., Hasse, J.M., and Avesar, D. (2013). A sodium-pump-mediated afterhyperpolarization in pyramidal neurons. J. Neurosci. 33, 13025–13041. https://doi.org/10.1523/JNEUROSCI.0220-13.2013.

47. Bhattacharjee, A., and Kaczmarek, L.K. (2005). For K+ channels, Na+ is the new Ca2+. Trends Neurosci. 28, 422–428. https://doi.org/10.1016/j.tins.2005.06.003.

48. Sun, B., Xu, P., Wang, W., and Salvaterra, P.M. (2001). In vivo modification of Na(+),K(+)-ATPase activity in Drosophila. Comp. Biochem. Physiol. B Biochem. Mol. Biol. 130, 521–536. https://doi.org/10.1016/s1096-4959(01)00470-5.

49. Dolan, M.J., Belliart-Guérin, G., Bates, A.S., Frechter, S., Lampin-Saint-Amaux, A., Aso, Y., Roberts, R.J.V., Schlegel, P., Wong, A., Hammad, A., et al. (2018). Communication from learned to innate olfactory processing centers is required for memory retrieval in Drosophila. Neuron 100, 651–668.e8. https://doi.org/10.1016/j.neuron.2018.08.037.

50. Lerner, H., Rozenfeld, E., Rozenman, B., Huetteroth, W., and Parnas, M. (2020). Differential role for a defined lateral horn neuron subset in naive odor valence in Drosophila. Sci. Rep. 10, 6147. https://doi.org/10.1038/s41598-020-63169-3.

51. Eschbach, C., Fushiki, A., Winding, M., Afonso, B., Andrade, I.V., Cocanougher, B.T., Eichler, K., Gepner, R., Si, G., Valdes-Aleman, J., et al. (2021). Circuits for integrating learned and innate valences in the insect brain. eLife 10, e62567. https://doi.org/10.7554/eLife.62567.

52. Kadakia, N., Demir, M., Michaelis, B.T., DeAngelis, B.D., Reidenbach, M.A., Clark, D.A., and Emonet, T. (2022). Odour motion sensing enhances navigation of complex plumes. Nature 611, 754–761. https://doi.org/10.1038/s41586-022-05423-4.

53. Brudner, S., Zhou, B., Jayaram, V., Santana, G.M., Clark, D.A., and Emonet, T. (2025). Fly navigational responses to odor motion and gradient cues are tuned to plume statistics. Preprint at bioRxiv. https://doi.org/10.1101/2025.03.31.646361.

54. Dolan, M.-J., Frechter, S., Bates, A.S., Dan, C., Huoviala, P., Roberts, R.J.V., Schlegel, P., Dhawan, S., Tabano, R., Dionne, H., et al. (2018). Neurogenetic dissection of the Drosophila innate olfactory processing center. Preprint at bioRxiv. https://doi.org/10.1101/404277.

55. Kitamoto, T. (2001). Conditional modification of behavior in Drosophila by targeted expression of a temperature-sensitive shibire allele in defined neurons. J. Neurobiol. 47, 81–92. https://doi.org/10.1002/neu.1018.

56. Badel, L., Ohta, K., Tsuchimoto, Y., and Kazama, H. (2016). Decoding of context-dependent olfactory behavior in Drosophila. Neuron 91, 155–167. https://doi.org/10.1016/j.neuron.2016.05.022.

57. Shuai, Y., Sammons, M., Sterne, G.R., Hibbard, K.L., Yang, H., Yang, C.-P., Managan, C., Siwanowicz, I., Lee, T., Rubin, G.M., et al. (2025). Driver lines for studying associative learning in Drosophila. eLife 13, RP94168. https://doi.org/10.7554/eLife.94168.

58. Benda, J. (2021). Neural adaptation. Curr. Biol. 31, R110–R116. https://doi.org/10.1016/j.cub.2020.11.054.

59. Handler, A., and Ginty, D.D. (2021). The mechanosensory neurons of touch and their mechanisms of activation. Nat. Rev. Neurosci. 22, 521–537. https://doi.org/10.1038/s41583-021-00489-x.

60. Rospars, J.P., Sanda, P., Lansky, P., and Duchamp-Viret, P. (2013). Responses of single neurons and neuronal ensembles in frog first- and second-order olfactory neurons. Brain Res. 1536, 144–158. https://doi.org/10.1016/j.brainres.2013.05.018.

61. Meeks, J.P., Arnson, H.A., and Holy, T.E. (2010). Representation and transformation of sensory information in the mouse accessory olfactory system. Nat. Neurosci. 13, 723–730. https://doi.org/10.1038/nn.2546.

62. Tan, J., Savigner, A., Ma, M., and Luo, M. (2010). Odor information processing by the olfactory bulb analyzed in gene-targeted mice. Neuron 65, 912–926. https://doi.org/10.1016/j.neuron.2010.02.011.

63. Niven, J.E., and Laughlin, S.B. (2008). Energy limitation as a selective pressure on the evolution of sensory systems. J. Exp. Biol. 211, 1792–1804. https://doi.org/10.1242/jeb.017574.

64. Barlow, H. (1961). Possible principles underlying the transformation of sensory messages. In Sensory Communication, W.A. Rosenblith, ed. (MIT Press), pp. 217–234.

65. Zocchi, D., Ye, E.S., Hauser, V., O'Connell, T.F., and Hong, E.J. (2022). Parallel encoding of CO(2) in attractive and aversive glomeruli by selective lateral signaling between olfactory afferents. Curr. Biol. 32, 4225–4239.e7. https://doi.org/10.1016/j.cub.2022.08.025.

66. Koyama, M., Minale, F., Shum, J., Nishimura, N., Schaffer, C.B., and Fetcho, J.R. (2016). A circuit motif in the zebrafish hindbrain for a two alternative behavioral choice to turn left or right. eLife 5, e16808. https://doi.org/10.7554/eLife.16808.

67. Tuthill, J.C., and Wilson, R.I. (2016). Parallel transformation of tactile signals in central circuits of Drosophila. Cell 164, 1046–1059. https://doi.org/10.1016/j.cell.2016.01.014.

68. Aldahabi, M., Balint, F., Holderith, N., Lorincz, A., Reva, M., and Nusser, Z. (2022). Different priming states of synaptic vesicles underlie distinct release probabilities at hippocampal excitatory synapses. Neuron 110, 4144–4161.e7. https://doi.org/10.1016/j.neuron.2022.09.035.

69. Aso, Y., Sitaraman, D., Ichinose, T., Kaun, K.R., Vogt, K., Belliart-Guérin, G., Plaçais, P.Y., Robie, A.A., Yamagata, N., Schnaitmann, C., et al. (2014). Mushroom body output neurons encode valence and guide memory-based action selection in Drosophila. eLife 3, e04580. https://doi.org/10.7554/eLife.04580.

70. Li, Q., and Liberles, S.D. (2015). Aversion and attraction through olfaction. Curr. Biol. 25, R120–R129. https://doi.org/10.1016/j.cub.2014.11.044.

71. Gupta, N., and Stopfer, M. (2012). Functional analysis of a higher olfactory center, the lateral horn. J. Neurosci. 32, 8138–8148. https://doi.org/10.1523/JNEUROSCI.1066-12.2012.

72. Litwin-Kumar, A., and Turaga, S.C. (2019). Constraining computational models using electron microscopy wiring diagrams. Curr. Opin. Neurobiol. 58, 94–100. https://doi.org/10.1016/j.conb.2019.07.007.

73. Scheffer, L.K., Xu, C.S., Januszewski, M., Lu, Z., Takemura, S.Y., Hayworth, K.J., Huang, G.B., Shinomiya, K., Maitlin-Shepard, J., Berg, S., et al. (2020). A connectome and analysis of the adult Drosophila central brain. eLife 9, e57443. https://doi.org/10.7554/eLife.57443.

74. Pologruto, T.A., Sabatini, B.L., and Svoboda, K. (2003). ScanImage: flexible software for operating laser scanning microscopes. Biomed. Eng. OnLine 2, 13. https://doi.org/10.1186/1475-925X-2-13.

75. Gohl, D.M., Silies, M.A., Gao, X.J., Bhalerao, S., Luongo, F.J., Lin, C.C., Potter, C.J., and Clandinin, T.R. (2011). A versatile in vivo system for directed dissection of gene expression patterns. Nat. Methods 8, 231–237. https://doi.org/10.1038/nmeth.1561.

76. Jin, L., Han, Z., Platisa, J., Wooltorton, J.R.A., Cohen, L.B., and Pieribone, V.A. (2012). Single action potentials and subthreshold electrical events imaged in neurons with a fluorescent protein voltage probe. Neuron 75, 779–785. https://doi.org/10.1016/j.neuron.2012.06.040.

Current Biology
Article

CellPress

77. Couto, A., Alenius, M., and Dickson, B.J. (2005). Molecular, anatomical, and functional organization of the Drosophila olfactory system. Curr. Biol. *15*, 1535–1547. https://doi.org/10.1016/j.cub.2005.07.034.

78. Goodman, M.B., and Lockery, S.R. (2000). Pressure polishing: a method for re-shaping patch pipettes during fire polishing. J. Neurosci. Methods *100*, 13–15. https://doi.org/10.1016/s0165-0270(00)00224-7.

79. Gouwens, N.W., and Wilson, R.I. (2009). Signal propagation in Drosophila central neurons. J. Neurosci. *29*, 6239–6249. https://doi.org/10.1523/JNEUROSCI.0764-09.2009.

80. Costa, M., Manton, J.D., Ostrovsky, A.D., Prohaska, S., and Jefferis, G.S. X.E. (2016). NBLAST: rapid, sensitive comparison of neuronal structure and construction of neuron family databases. Neuron *91*, 293–311. https://doi.org/10.1016/j.neuron.2016.06.012.

81. Pereira, T.D., Tabris, N., Matsliah, A., Turner, D.M., Li, J., Ravindranath, S., Papadoyannis, E.S., Normand, E., Deutsch, D.S., Wang, Z.Y., et al. (2022). SLEAP: A deep learning system for multi-animal pose tracking. Nat. Methods *19*, 486–495. https://doi.org/10.1038/s41592-022-01426-1.

82. Murlis, J., Elkinton, J.S., and Cardé, R.T. (1992). Odor plumes and how insects use them. Annu. Rev. Entomol. *37*, 505–532. https://doi.org/10.1146/annurev.en.37.010192.002445.

83. Jayaram, V., Kadakia, N., and Emonet, T. (2022). Sensing complementary temporal features of odor signals enhances navigation of diverse turbulent plumes. eLife *11*, e72415. https://doi.org/10.7554/eLife.72415.

84. Bates, A.S., Manton, J.D., Jagannathan, S.R., Costa, M., Schlegel, P., Rohlfing, T., and Jefferis, G.S. (2020). The natverse, a versatile toolbox for combining and analysing neuroanatomical data. eLife *9*, e53350. https://doi.org/10.7554/eLife.53350.

85. Cuntz, H., Forstner, F., Borst, A., and Häusser, M. (2010). One rule to grow them all: a general theory of neuronal branching and its practical application. PLoS Comput. Biol. *6*, e1000877. https://doi.org/10.1371/journal.pcbi.1000877.

86. Albrecht, D.G., and Hamilton, D.B. (1982). Striate cortex of monkey and cat: contrast response function. J. Neurophysiol. *48*, 217–237. https://doi.org/10.1152/jn.1982.48.1.217.

87. Heeger, D.J. (1992). Normalization of cell responses in cat striate cortex. Vis. Neurosci. *9*, 181–197. https://doi.org/10.1017/s0952523800009640.

88. Katz, B. (1969). The Release of Neural Transmitter Substances (Liverpool University Press).

89. Silver, R.A. (2003). Estimation of nonuniform quantal parameters with multiple-probability fluctuation analysis: theory, application and limitations. J. Neurosci. Methods *130*, 127–141. https://doi.org/10.1016/j.jneumeth.2003.09.030.

90. Kazama, H., and Wilson, R.I. (2008). Homeostatic matching and nonlinear amplification at genetically-identified central synapses. Neuron *58*, 401–413. https://doi.org/10.1016/j.neuron.2008.02.030.

91. Tobin, W.F., Wilson, R.I., and Lee, W.A. (2017). Wiring variations that enable and constrain neural computation in a sensory microcircuit. eLife *6*, e24838. https://doi.org/10.7554/eLife.24838.

92. McCarthy, E.V., Wu, Y., Decarvalho, T., Brandt, C., Cao, G., and Nitabach, M.N. (2011). Synchronized bilateral synaptic inputs to *Drosophila melanogaster* neuropeptidergic rest/arousal neurons. J. Neurosci. *31*, 8181–8193. https://doi.org/10.1523/JNEUROSCI.2017-10.2011.

STAR★METHODS

KEY RESOURCES TABLE

REAGENT or RESOURCE	SOURCE	IDENTIFIER
Chemicals, peptides, and recombinant proteins		
Ethyl acetate, $\geq$ 99.8%	Millipore-Sigma	Cat#: 270989
Methyl acetate, $\geq$ 99.8%	Millipore-Sigma	Cat#: 45999
Apple cider vinegar	Great Value	N/A
Paraffin oil	J.T. Baker	S894-07
Mouse anti brp	DSHB	nc82; RRID:AB_2314866
Goat anti-mouse Alexa Fluor 633	Invitrogen	A-21050; RRID:AB_141431
Deposited data		
Drosophila hemibrain v.1.2.1	https://neuprint.janelia.org	Scheffer et al.[73]
Electrophysiology and imaging data	This study	10.5281/zenodo.15625190
Experimental models: Organisms/strains		
D. melanogaster: P{UAS-mCD8::GFP.L}LL5 (II)	BDSC	RRID: BDSC_5137
D. melanogaster: P{UAS-mCD8::GFP.L}Ptp4E[LL4] (X)	BDSC	RRID:BDSC_5136
D. melanogaster: NP5221-Gal4 (II)	DGRC (Kyoto)	104–906
D. melanogaster: NP3062-Gal4 (X)	DGRC (Kyoto)	113-083
D. melanogaster: GH146-Gal4 (II)	BDSC	RRID: BDSC_30026
D. melanogaster: P{GMR37G11-GAL4}attP2	BDSC	RRID: BDSC_49539
D. melanogaster: P{GMR45F12-GAL4}attP2	BDSC	RRID: BDSC_50240
D. melanogaster: P{R38D01-p65.AD}attP40, P{R45F12-GAL4.DBD}attP2 (LH290-Gal4)	BDSC	RRID: BDSC_86710
D. melanogaster: P{R29G05-p65.AD}attP40, P{R37G11-GAL4.DBD}attP2 (LH989-Gal4)	BDSC	RRID: BDSC_86697
D. melanogaster: UAS-Unc13B-RNAi (III)	Atefeh Pooryasin and Stephan Sigrist	Fulterer et al.[42]
D. melanogaster: UAS-D369N (UAS-dnATPase) (III)	Leslie Griffith	Sun et al.[48]
D. melanogaster: +; UAS-shi[ts]; UAS-shi[ts]	Damon Clark	Kitamoto[55]
D. melanogaster: PBac{20XUAS-IVS-GCaMP6f}VK00005	BDSC	RRID: BDSC_52869
P{UAS-ArcLight}attP2 (III)	BDSC	RRID: BDSC_51056
P{UAS-ArcLight}attP40 (II)	BDSC	RRID: BDSC_51057
P{GAL4.DBD.Uw}attP2 (Empty split gal4) (III)	BDSC	RRID: BDSC_71209
P{Or42b-LexA}JK73A (III)	Marta Zlatic	Eschbach et al.[51]
PBac{13XLexAop2-IVS-CsChrimson.tdTomato}VK00005 (III)	BDSC	RRID: BDSC_82183
Software and algorithms		
MATLAB 2018a and 2021a	MathWorks	N/A
R 3.6.2	https://www.r-project.org/	N/A
R Studio 1.2.5033	https://www.r-project.org/	N/A
Python 3.9.5	https://www.python.org/	N/A
ScanImage 2018b-1	MBF Bioscience	Pologruto et al.[74]
HCImageLive	Hamamatsu Photonics	N/A
Neuprint	https://neuprint.janelia.org/	N/A
Neuprint-python	https://github.com/connectomeneuprint/neuprint-python	N/A
natverse	https://natverse.org/nat/	N/A
Custom matlab, python, and R scripts	This study	10.5281/zenodo.15625190

Current Biology
Article

 CellPress

EXPERIMENTAL MODEL AND STUDY PARTICIPANT DETAILS

Flies (*Drosophila melanogaster*) were raised on conventional cornmeal agar medium supplemented with rehydrated potato flakes (Carolina Biological Supply) and yeast under a 12 h light, 12 h dark cycle at 25°C. All electrophysiology experiments were performed *in vivo* on adult female flies either on the day of eclosion (at least 8 hours old) or one day after eclosion. Voltage and calcium imaging experiments were performed on adult female flies 1-4 days after eclosion. Behavior experiments were performed on adult female flies 4-5 days after eclosion. All flies used for behavior experiments were in the IsoD1 genetic background.[75]

The following genotypes were used:

Experiment	Genotypes
Voltage imaging from LHN1	; +/UAS-ArcLight; GMR37G11-Gal4/UAS-ArcLight;
Voltage imaging from LHN2	; LH290-Gal4/UAS-ArcLight; LH290-Gal4/UAS-ArcLight;
Calcium imaging from PNs	GH146-Gal4/+; UAS-GCaMP6f/+
Electrophysiology recordings from DM1 PNs	; NP5221-Gal4, UAS-CD8-GFP; or; NP5221-Gal4, UAS-CD8-GFP; GMR37G11-Gal4 or; NP5221-Gal4, UAS-CD8-GFP; GMR45F12-Gal4
Electrophysiology recordings from DM4 PNs	NP3062-Gal4, UAS-CD8-GFP;;
Electrophysiology recordings from LHN1 (no genetic perturbations)	; NP5221-Gal4, UAS-CD8-GFP; GMR37G11-Gal4
Electrophysiology recordings from LHN2 (no genetic perturbations)	; NP5221-Gal4, UAS-CD8-GFP; GMR45F12-Gal4 or; LH290-Gal4 / 20x-UAS-GFP
Paired electrophysiology recordings from DM1 and LHN1	; NP5221-Gal4, UAS-CD8-GFP; GMR37G11-Gal4
Paired electrophysiology recordings from DM1 and LHN1	; NP5221-Gal4, UAS-CD8-GFP; GMR45F12-Gal4
Electrophysiology recordings from LHN1 with dominant negative Na+/K+ ATPase	10x-UAS-GFP / +; GMR37G11-Gal4 / UAS-dnATPase
Electrophysiology recordings from LHN2 with Unc13B knockdown	; NP5221-Gal4, UAS-CD8-GFP; GMR45F12-Gal4 / UAS-Unc13B-RNAi or; LH290-Gal4/NP5221-Gal4, UAS-CD8-GFP; LH290-Gal4 / UAS-Unc13B-RNAi
Electrophysiology recordings from LHN1 with Unc13B knockdown	; NP5221-Gal4, UAS-CD8-GFP / +; GMR37G11-Gal4 / UAS-Unc13B-RNAi
Control LHN2 recordings for Unc13B knockdown	; NP5221-Gal4, UAS-CD8-GFP; GMR45F12-Gal4 or; 10x-UAS-GFP / +; GMR45F12-Gal4 / UAS-Unc13B-RNAi
Control LHN1 recordings for Unc13B knockdown	; NP5221-Gal4, UAS-CD8-GFP; GMR37G11-Gal4 or; 10x-UAS-GFP / +; GMR37G11-Gal4 / UAS-Unc13B-RNAi
Behavior experiments, LH290 control	+; R38D01-AD/+; R45F12-DBD/Or42b-LexA, LexAop-CsChrimson
Behavior experiments, LH290 silenced	+; R38D01-AD/UAS-Shibire; R45F12-DBD/Or42b-LexA, LexAop-CsChrimson
Behavior experiments, LH989 control	+; R29G05-AD/+; R37G11-DBD/Or42b-LexA, LexAop-CsChrimson
Behavior experiments, LH989 silenced	+; R29G05-AD/UAS-Shibire; R37G11-DBD/Or42b-LexA, LexAop-CsChrimson
Behavior experiments, SS01372 control	+; R25B07-AD/+; R55F01-DBD/Or42b-LexA, LexAop-CsChrimson
Behavior experiments, SS01372 silenced	+; R25B07-AD/UAS-Shibire; R55F01-DBD/Or42b-LexA, LexAop-CsChrimson
Behavior experiments, LH991 control	+; R29G05-AD/+; R37G11-DBD/Or42b-LexA, LexAop-CsChrimson
Behavior experiments, LH991 silenced	+; R29G05-AD/UAS-Shibire; R37G11-DBD/Or42b-LexA, LexAop-CsChrimson
Behavior experiments, UAS control	+; +/UAS-Shibire; +/Or42b-LexA, LexAop-CsChrimson

METHOD DETAILS

Fly preparation for imaging and electrophysiology

For odor coding experiments, each fly was cold-anesthetized, positioned into a small holder made of stainless steel shim stock (0.001″ thick), and affixed into position using paraffin wax such that the antennae were under the foil and dry while the head and brain was bathed in external saline. The external saline contained (in mM): 103 NaCl, 3 KCl, 5 N-tris(hydroxymethyl) methyl-2-aminoethane-sulfonic acid, 8 trehalose, 10 glucose, 26 $NaHCO_3$, 1 NaH_2PO_4, 1.5 $CaCl_2$ and 4 $MgCl_2$ (osmolarity adjusted to 270–275 mOsm). A small window in the top of the head capsule was dissected using electrolytically sharpened tungsten wires and fine forceps. Fat, air sacs, and trachea were removed from above the brain. Fine forceps were then used to gently remove the perineurial sheath only above the area of the brain housing the target somata. Large-bore cleaning pipettes were used to remove residual glia and interfering somata to gain clear access to target somata. External saline was bubbled with 95% O_2 and 5% CO_2 and reached an equilibrium pH of 7.3. Saline was superfused continuously over the brain during recording.

Voltage Imaging

In vivo voltage imaging of LHNs (Figures S1C, S1D, S3A–S3C, S3I, and S3J) was performed on an upright epifluorescence micro-scope (Scientifica Slicescope) and placed under a 40x 0.8NA water-immersion objective lens (Olympus). Arclight[76] was excited with a 470 nm LED at 2.4% power (CoolLED pE-100), yielding 0.282 mW at the sample. Arclight fluorescence emission was collected with a scientific CMOS camera (Hamamatsu C1140-42U30), operating under HCImageLive software at an acquisition rate of 100 frames per second.

Calcium Imaging

In vivo calcium imaging of PNs (Figures S2C and S2D) was performed on a 2-photon laser scanning microscope (Scientifica MP-2000) using a 20x 1.0NA water-immersion objective lens (Olympus). A Titanium-Sapphire laser was tuned to 920nm to excite GCaMP6f, and fluorescence emission was collected with a GaAsP PMT, controlled by ScanImage software (MBF Bioscience). Im-ages were collected at an acquisition rate of 16.9 frames per second. Measurements from multiple z-slices through the antennal lobe were collected sequentially for each fly. DM1, DM4, and other glomeruli were identified based on established landmarks.[77] dF/F was calculated as the increase in fluorescence per glomerulus during odor presentation, normalized by the baseline fluorescence in the corresponding glomerulus. No substantial activity was observed outside of DM1 and DM4 in these experiments.

Specificity of genetic manipulations

Disruption of the Na+/K+ ATPase was performed by expressing dnATPase only with the LHN1 driver line (R37G11-Gal4). This line does not express in the DM1 (or any other) PN, so this manipulation is specific to LHN1.

Knockdown of Unc13B was performed by expressing Unc13B-RNAi in DM1 PNs using the DM1 driver line (NP5221-Gal). However, we also needed to express GFP in LHN1 or LHN2. Because of genetic constraints, this meant that the manipulation also knocked down Unc13B in LHNs (since driver lines for both PNs and LHNs used the Gal4/UAS system). Nonetheless our manipulation should not have any direct effects on LHN physiology in our experimental configuration, because Unc13 occurs only at presynapses.[40] Accordingly, we did not see any effects of Unc13B knockdown on LHN responses to low concentrations of methyl acetate (which activates DM4 but not DM1 PNs) or on intrinsic LHN2 excitability. In addition, in some experiments we expressed Unc13B-RNAi only in LHN2 (and not in DM1), and these manipulations had no effect on ethyl acetate responses in LHN2. These data are included in the control datasets in Figure 5. Thus, in our experiments, the manipulation of Unc13B should affect LHN responses only through presynaptic effects of the DM1 PN.

The Unc13B-RNAi line that we use has been validated by multiple labs to specifically reduce expression of Unc13B (and not affect Unc13A expression); the effects we observe with Unc13B knockdown are consistent with its role at other synapses.[42,43] However, reagents are not available to confirm phenotypic stability with a different RNAi target sequence or to perform genetic rescue, so it is formally possible that the effects of this genetic manipulation may be partly due to off-target effects on other genes.

Electrophysiology

Recordings were obtained using an Olympus BX51 upright microscope with 40X water immersion objective. One PN or LHN was recorded per fly, except for paired recordings. Patch-clamp electrodes were filled with an internal solution of (in mM): KCH_3SO_3H 160, HEPES 10, MgATP 4, Na_3GTP 0.5, EGTA 1, biocytin hydrazide 13 (pH = 7.3, adjusted to 265mOsm). For paired recordings, EGTA was omitted from the internal solution in the PN pipette, except when explicitly stated otherwise. All other recordings included 1mM EGTA. Patch pipettes were made from borosilicate glass (Sutter; 1.5-mm outer diameter, 0.86-mm inner diameter) and were pulled and pressure polished[78] to create a relatively long taper with final pipette tip opening of about 0.75μm in diameter. This enabled high seal resistances (>50GΩ), which helped keep leak currents negligible in LHNs, which typically have input resistances of 2-5 GΩ. Spike amplitudes in LHN recordings were 5-10mV and spike amplitudes in PN recordings were 15-25mV. Recordings were obtained with Axopatch 200B model amplifiers in current clamp mode with CV-203BU head stages, digitized at 10-30kHz with an analog-to-digital converter (National Instruments), and saved to disk using the MATLAB data acquisition toolbox. Recordings were not cor-rected for a liquid junction potential of ∼13mV.[79]

Paired PN-LHN recordings were conducted with the fly head rotated 90 degrees so that one eye was directed up. The eye and optic lobe were removed, along with the ipsilateral antenna to improve physical access to PNs. This configuration was necessary for recording pipettes to access both PN and LHN2 cell bodies because they are nearly antipodal to each other in the anterior-posterior

Current Biology
Article

CellPress

and dorsal-ventral axes but are both lateral. Although DM1 and LHN1 cell bodies are in locations that are compatible with preserving both antennae,[13] we used the same head orientation for both sets of paired recordings here to minimize differences between experiments.

Current was applied to DM1 via the patch clamp amplifier (in current clamp mode) in 100 msec pulses at 5Hz (i.e., 100 msec intervals between pulses). A single exception was one DM1-LHN2 recording (with EGTA) where pulses were 60msec. Pulse amplitude was 100-300pA, determined empirically for each PN to evoke at least 5 spikes per pulse. The current amplitude was kept the same after dialysis, except for one pair where the amplitude was slightly increased. For square wave current injections into the PN, the series resistance was estimated from the fastest time constant of depolarization and subtracted from recorded PN voltage waveforms. Series resistance correction was imperfect during brief transient windows (<10msec in duration) at current onset and offset, so voltage data were interpolated from surrounding values during these times.

For all paired experiments, the recording from the LHN was established first, and then the DM1 recording was established. This allowed immediate measurements of synaptic potentials in the paired configuration before PN dialysis. Because the contralateral antenna remained intact, odor stimulation could still drive responses. In one DM1-LHN2 paired recording (with EGTA), we used a solid 2 seconds of ethyl acetate stimulation (1e-6× concentration) instead of pulsed current injection. This pair is included in Figures 4G–4J (analyzing only the first 100msec of the response) and in Figure 4L, but not in Figures 4E, 4F, and 4K because the temporal stimulus profile was different.

We note that 1mM EGTA is commonly included in internal saline recipes in *Drosophila* experiments. While EGTA does not appear to affect a cell's integration of synaptic inputs and spike generation (as measurable from the soma), it clearly disrupts some synaptic outputs. Thus, we recommend omitting EGTA from internal saline during any patch-clamp recording where perturbation to its synaptic outputs is not desired (e.g., during simultaneous measurement of components of downstream network activity or of behavior).

Following most LHN recordings, brains were processed for immunohistochemistry exactly as described previously,[14] and imaged with a Zeiss LSM 880 confocal microscope to visualize the biocytin fill. All filled cells of each LHN type were morphologically alike to a degree expected of a single cell type.[12,80] No recordings were omitted based on this recovered morphology.

Freely moving walking behavior

Flies were prepared and tested using a custom-built wind tunnel, as described by Kadakia et al.[52] Briefly, around forty 1–2 day-old females were anesthetized with CO_2 and food-deprived for 72h in polystyrene vials (Genesee #32-110) capped with Flugs (Genesee #49-191). A ~3 mm slice was cut from the end of a Flug, soaked in deionized water, and placed at the bottom of each vial. Food-deprived flies had water available ad libitum. For optogenetic experiments, 500 μL of 2 mM all-trans-Retinal (Sigma-Aldrich, R2500) diluted in water was added 24 hours before testing, and the vials were kept in the dark until the experiment. Prior to transferring flies into the arena, vials were placed in a temperature-controlled incubator (PHCbi Cooled Incubators) set to 36°C for 30 minutes.

The custom-built wind tunnel arena measured 270 x 170 mm^2, allowing flies to walk freely. Constant laminar airflow was maintained at 150 mm/s. Throughout the arena, green light (Luxeon Rebel LED 530 nm) was used to flood the visual system, effectively preventing any visual responses to red light.[52] Behavior was recorded at 60 Hz using a FLIR Grasshopper USB 3.0 NIR camera, and trajectories were extracted using SLEAP.[81] A seedling mat (Vivosun Seedling Mat with Thermostat) placed under the glass floor maintained the surface temperature at 30°C; this temperature was confirmed to be effective for *Shibire* by crossing UAS-Shibire with nSyb-Gal4, which resulted in complete paralysis of flies containing both transgenes.

For optogenetic stimulation, full-field flashes of red light were presented at 60 Hz using a projector (Texas Instruments DLPLCR4500EVM) mounted on top of the arena. Custom Python scripts controlled the stimulus presentation. Each trial consisted of a 16-second stimulus period followed by 16 seconds with no stimulus. The 16-second stimulus block began with flashes at 5 Hz (100 ms duration) and then switched to either 2.5 Hz or 10 Hz (100 ms duration), with the transition choice randomly selected for each repeat. Each trial was repeated four times, followed by a one-minute intermission before repeating four additional times. Overall, each set of flies was tested for up to forty trials (approximately 30 minutes).

Odor delivery and stimulus design

A clean air stream (1360 mL/min) was filtered through activated carbon and directed to the fly through a carrier tube (Figure S2A). Separate air streams of 12 ml/min were directed under the control of a solenoid valve (The Lee Company, model LHDA1231415H) into the headspace of 2mL vials (Thermo Scientific, National C4011-5W) containing odors. The odor streams joined the carrier stream 9–11 cm from the end of the tube. All experiments, except for those in Figures 6A and 6B used the odor delivery configuration in Figure S2A (one solenoid valve per odor vial and predominantly Tygon tubing). The experiments in Figures 6A and 6B used the odor delivery configuration in Figure S2B (two solenoid valves per odor vial and predominantly PTFE tubing). In some experiments, a digital camera (Basler ace acA1300-200um) was set up facing the lateral side of the prep, to facilitate uniform positioning of the carrier tube relative to the fly antennae across experiments.

Odors were prepared by serial dilution in either paraffin oil or water. Ethyl acetate and methyl acetate were used at 1e-6× dilution, except in Figures S3G and S3H. To ensure sufficient headspace in each odor vial, the final volume of odor dilutions was 0.5 mL.

Odors were delivered in repeated pulses for three reasons. First, they loosely model the intermittent patterns of natural odor plumes carried by wind.[82] Increases in pulse frequency can signal increasing proximity to the odor source.[83] Second, they allow for a relatively simple and convenient way to experimentally manipulate the time-averaged odor intensity while remaining in a private odor

regime. Third, they provide an additional layer of temporal diversity in the neural activity patterns, which is useful for constraining linear filter models (Figures 2, 5, and 6).

The timing of valve opening and closing was controlled by a custom MATLAB script. Each odor pulse was controlled by opening the valve for 40msec, except for the experiments in Figures 6A and 6B, where valves were opened for 150msec. The longer duration was necessary because the two-valve odor delivery system required more time for odor to reach the fly. Because two odors were simultaneously connected to the carrier stream and were independently controllable, we alternated odor identity from trial to trial and interleaved odor pulse frequencies, to minimize effects of any slow changes in neural responses over the course of each experiment.

For characterization of unadapted odor tuning curves for each neuron type, odors were delivered in 40msec pulses at 0Hz (i.e., spontaneous activity) 1Hz, 2.5Hz, 5Hz, and 10Hz, each following at least 10 seconds without any odor stimulation. 10 pulses were delivered for 1Hz stimulation, 20 pulses for 2.5Hz, and 30 pulses for 5 and 10Hz stimulation. To measure adapted odor tuning curves, 20 seconds of pulsed odor stimuli were delivered at adapting frequencies of 1, 2.5, or 5Hz, and then odor pulse frequency was immediately changed to the "test" frequency of 1, 1.5, 2, 2.5, 3, 3.5, 5, 7.5, or 10Hz for 10 seconds. Test frequencies of 1.5, 2, 3, 3.5 and 7.5Hz were not tested for every adapting frequency. For cross-adaptation experiments (Figure S5), the adapting frequency was always 5Hz (of ethyl acetate).

Valve switching introduced brief and small electrical artifacts in electrophysiology voltage traces. These were most evident for the high input resistance neurons (LHNs) where small noise currents cause proportionally large voltage deflections. For display purposes only, we removed these artifacts by blanking the voltage for 10-12msec after each valve switching event and linearly interpolating to fill the gap.

Immunohistochemistry and imaging

Adult Drosophila brains and ventral nerve cords were dissected in ice-cold external saline and fixed in 4% paraformaldehyde (w/v in PBS) for 20 minutes at room temperature. Following fixation, brains were washed three times with PBS-T [PBS containing 0.5% (v/v) Triton X-100; Sigma Aldrich, #X100], then incubated overnight at 4°C with primary antibodies diluted in 0.4% PBS-T supplemented with 10% Normal Goat Serum. After three washes with PBS-T, brains were incubated overnight at 4°C with secondary antibodies, also diluted in 0.4% PBS-T with 10% Normal Goat Serum. Samples were then washed three times for 15 minutes each in PBS and mounted in Vectashield H-1000 (Vector Laboratories, Burlingame, CA) anti-fade mounting medium for confocal microscopy. The primary antibody was mouse anti-brp (used in a 1:250 dilution). The secondary antibody was goat anti-mouse 633 (used in a 1:500 dilution). Imaging was performed using a Zeiss LSM 880 confocal microscope. Image stacks were acquired at a resolution of 1024 × 1024 pixels with a z-step size of 0.5 μm using a 40× objective lens.

QUANTIFICATION AND STATISTICAL ANALYSIS

Connectome analysis

Synaptic connectivity data were obtained from the Hemibrain connectome (version 1.2.1) using custom Python scripts and the neuprint-python API. Synapse counts between all canonical cholinergic uniglomerular PNs (those in the adPN or lPN lineages) and each instance of LHN1 and LHN2 were retrieved with "fetch_adjacencies." For analysis of PN outputs (Figure S1A), raw synapse counts were normalized by total PN output synapses. For analysis of LHN inputs (Figure S1B), raw synapse counts were normalized by the total number of input synapses on each LHN instance. Reciprocal connections onto LHN1 (Figure 6C) were identified similarly, and raw synapse counts were normalized by total synapse count of the recipient neuron. Synapse location and cellular morphology data (Figure S6) were obtained from the same connectome using custom R scripts using the "hemibrain_extract_synapses" and "hemibrain_read_neurons" functions of the natverse toolbox.[84] Euclidean and geodesic distances between all pairs of synapses on PN axon arbors were computed using the TREES toolbox for MATLAB.[85]

Spike identification, analysis of spike rates, and analysis of membrane voltages

Prior to spike detection, raw voltage traces were highpass filtered with a second-order digital Butterworth filter with cutoff frequency of 5Hz and then lowpass filtered with a second-order digital Butterworth filter with cutoff frequency of 500Hz. Spikes were detected as negative threshold crossings of the second derivative of the filtered voltage trace. The threshold was adjusted for each recording. Because recording conditions can change slightly over time, every threshold crossing was inspected to remove artifactual false positive crossings. Artifactual false negatives were manually added back in. Most of the false positive crossings were the result of valve switching artifacts described above (to ensure every spike was detected, spike detection was performed without removal or interpolation of these artifacts).

Peristimulus time histograms (PSTHs) were computed by binning spike times into 50msec bins. All repeated trials for each stimulus were combined into a single average PSTH for that neuron and stimulus. For all unadapted odor-tuning curves and cellular input-output functions, the transient responses for each stimulus were computed as the average spike rate in the first 1 second of the response. For adapted tuning curves, the transient responses were computed as the average spike rate in the first 1 second after switching to the new odor pulse frequency. Because our odor delivery system required about 100msec for odor to flow from the vial to the fly (Figure S1), we shifted each response window (relative to valve timing) by 100msec to account for this. Trough voltages

Current Biology
Article

CellPress

(Figures 6A and 6B) were measured as the average membrane voltage in 50msec windows starting 750msec after the response to each odor pulse (i.e., the 50msec just prior to the depolarizing response to the next odor pulse).

Curve fitting to odor tuning curves and cellular input-output functions

Unadapted odor tuning curves (functions relating odor pulse rate to spike rate) and cellular input-output functions (relating PN spike rates to LHN spike rates) were fit with the saturating hyperbolic ratio function[26,86]

$$R(i) \; = \; R_{max}\frac{(i \, - \, \mu)^2}{\sigma^2+(i \, - \, \mu)^2}$$

where the variable i is the input (PN spike rate or odor pulse rate) and R is the output (PN or LHN spike rate). R_{max} represents the saturation value of the function, μ represents the subtractive input offset, and σ determines the divisive input gain; all three parameters were fitted to data. Divisive adaptation was modeled by adjusting σ (a standard model of divisive gain control[87]) and subtractive adaptation was modeled by adjusting μ. Fits to adapted data were carried out by freezing R_{max} at the value fitted to unadapted data and then refitting both both μ and σ. For all adapted fits, R was set to zero for $i < \mu$, and μ and σ were each constrained to be equal or larger than the corresponding fit to unadapted data (to avoid spurious multiplicative or additive modulation fits).

Measures of deviation from linearity (Figures 2G–2I and 5H–5J) were computed by fitting a linear model to the responses to the lowest 4 test stimuli (0, 1, 2.5, and 5Hz) for each LHN individually (as a function of average DM1 spike rates). We then compared the LHN response to the 10Hz stimulus to that predicted by the linear model. The gain ratio (Figure 6M) was computed as the ratio of the gain for linear regression for stimulus frequencies between 0 and 10Hz for adapted responses and the gain for linear regression for stimulus frequencies between 0 and 5Hz unadapted responses. The stimulus domains used for regression was different in order to only capture the linear regime of responses (in the unadapted case, the 10Hz stimulus began to engage the saturating nonlinearity which we did not consider in this analysis).

Analysis of LHN coding of proportional (stimulus ratio) and absolute (stimulus difference) changes in odor pulse frequency (Figures 5K, 6N, 6O, S4C, and S4F) were performed by either dividing the test frequency by the adapting frequency or subtracting the adapting frequency from the test frequency prior to plotting the odor tuning curves. For the analysis of stimulus ratio, all test frequencies for 2.5Hz and 5Hz adaptation frequencies are shown (and included in the linear fits). However, the two highest test frequencies for 1Hz adaptation are omitted because these started to engage the saturating nonlinearity, which we did not consider in this analysis. For Figures 6N, 6O, S4C, and S4F, linear models were fit to data for each adapting frequency separately, but only nonzero responses were included for fits for LHN2, again to focus on the linear spike rate regime. The ANCOVA test was used to determine whether a single model relating LHN spike rate to proportional changes or absolute differences in odor pulse rate could be rejected.

Dynamic linear filter models and voltage-spiking analysis

The dynamic linear model predicting LHN membrane potential from DM1 spike times in Figures 2 and 5 was based on a "synaptic" filter shape following an alpha function of the form

$$V_m(t) \; = \; \beta_1(t \, / \, \beta_2)e^{-t/\beta_2}$$

β_1 and β_2 determine the amplitude and timecourse of the filter, respectively. The filter was then convolved with a series of delta functions representing DM1 spike times to produce a predicted continuous membrane potential. In other words, the model assumed that every DM1 spike generated an LHN voltage deflection following the filter function and overlapping voltage deflections were summed linearly. Values of β_1 and β_2 were fitted to the mean membrane potential response for each LHN recording, using the lsqcurvefit function in the MATLAB optimization toolbox. The corresponding fits to LHN1 voltages in Figure 6 used a filter composed of a linear combination of two alpha functions:

$$V_m(t) \; = \; \beta_1\left(\frac{t}{\beta_2}\right)e^{-\frac{t}{\beta_2}} + \beta_3\left(\frac{t}{\beta_4}\right)e^{-\frac{t}{\beta_4}}$$

where β_3 was constrained to be negative.

To assess the relationship between mean membrane potential and spike rate, the entire 45 second recording of LHN responses to the 5Hz-10Hz stimulus (including activity before and after stimulus presentation) was used. Mean voltages and spike rates (across recordings) were binned into 200 msec bins and the relationship between them was modeled with an exponential function of the form

$$FR(V_m) \; = \; \beta_1\left(e^{\beta_2(V_m - \beta_3)}\right)$$

β_1, β_2 and β_3 were fit to data using the lsqcurvefit function in the MATLAB optimization toolbox.

Synaptic data analysis

Unitary excitatory postsynaptic potential (uEPSPs) waveforms were measured from the LHN membrane voltage in a brief time window surrounding each DM1 PN spike time (starting 1msec prior to the PN spike until 10msec after the PN spike). If the LHN generated a spike during this time window, the uEPSP waveform was omitted from all further analysis. In a few cases, LHNs were gently hyperpolarized by 5-10mV with tonic current injection to reduce likelihood of spiking. uEPSP amplitudes were computed as the maximum net depolarization within the uEPSP waveform.

For the analysis of EGTA effects, pre-dialysis measurements were all taken within 8 minutes of establishing the PN whole cell patch clamp configuration (mean: 3.3 minutes). Post-dialysis measurements were all taken after at least 12 minutes of establishing the PN whole cell patch clamp configuration (mean: 33.5 minutes). Synaptic responses remained stable following dialysis.

We used quantal theory to estimate the initial release probability and quantal content of PN-LHN synapses (Figure 3E). Quantal theory relates the mean synaptic current amplitude to the number of release sites (N), probability of release at each site (P), and the quantal size of each release event (Q)[88]

$$I = NPQ.$$

Assuming a binomial model,[89] the variance of the synaptic current amplitude (over repeated trials) is

$$\sigma^2 = NQ^2P(1 - P).$$

In *Drosophila*, the number of release sites estimated by quantal theory[90] closely matches the number of physical synapses measured with electron microscopy.[91] Thus, we used synapse counts from the Hemibrain connectome to estimate the mean N for each synapse type (43.0 ± 8.4 for DM1-LHN1, and 18.8 ± 4.4 for DM1-LHN2; incidentally, our biocytin fills indicated that this LHN1 sample only included the PD2a1 subtype, so estimates were taken only from that subtype in the Hemibrain).[73] This allows P and Q to be calculated from the equations above using experimental measurements of the mean and variance of EPSP amplitude (without experimental manipulation of release probability). Because quantal theory predicts the amplitude of synaptic current instead of voltage (our experiments only measured voltage), we estimated EPSC amplitude by dividing EPSP amplitude by the average input resistance for each cell type (2.7 ± 0.5 GΩ for LHN1, 4.1 ± 0.9 GΩ for LHN2). We only analyzed the first EPSP in the first pulse of each trial and verified that none of these responses evoked spikes in the LHN.

Model of short-term plasticity at PN-LHN synapses

Synaptic responses in LHN1 were modeled using a depression-only version of the Tsodyks-Markram model defined as follows[33]:

$$\frac{dx(t)}{dt} = \frac{z(t)}{\tau_{rec}} - U_{SE}x(t)\delta(t - t_{sp})$$

$$\frac{dy(t)}{dt} = \frac{y(t)}{\tau_{inact}} - U_{SE}x(t)\delta(t - t_{sp})$$

$$\frac{dz(t)}{dt} = \frac{y(t)}{\tau_{in}} - \frac{z(t)}{\tau_{rec}}$$

The dynamic variables x, y, and z represent the fraction of resources in recovered, active and inactive states, respectively. δ denotes the Kronecker delta function, which evaluates to 1 when the input is 0 and evaluates to 0 for all other inputs. U_{SE} denotes the "utilization of synaptic efficacy," which is the fraction of available resources used per spike. t_{sp} denotes the time of each DM1 spike. τ_{inact} is the time constant of inactivation, which determines the timecourse of the unitary synaptic current and was fixed at 3msec.[33] In this model, the synaptic current is proportional to y(t). Because our experiments measured synaptic voltage instead of current, we also simulated the passive dynamics of the postsynaptic membrane as follows:

$$\frac{dV_m(t)}{dt} = -\frac{(V_m(t) - V_r)}{R_mC_m} + \frac{y(t)A_{SE}(V_m(t) - E_{ACh})}{C_m}$$

Rm and Cm are the membrane resistance and capacitance, respectively. V_r is the resting potential of the neuron and was set at -50mV. E_{ACh} is the synaptic reversal potential for acetylcholine receptors and was set to -10mV.[92] A_{SE} is the maximal synaptic strength and serves as a scaling factor. For LHN1, R_m was set to 2.7GΩ based on our experimental measurements and C_m was estimated at 20pF based on the neuron's size. The parameters τ_{rec} (the time constant of recovery from depression), U_{SE}, and A_{SE} were jointly optimized to minimize the mean squared error of each uEPSP amplitude, using the lsqcurvefit function of the MATLAB optimization toolbox.

Synaptic responses in LHN2 were modeled in the same way as LHN1, except that U_{SE} increased with each spike and decayed with a characteristic time constant, to account for synaptic facilitation.[33] This introduced an additional dynamic model variable:

$$\frac{dU_{SE}(t)}{dt} = -\frac{U_{SE}(t)}{\tau_{facil}} + U'_{SE}(1 - U_{SE}(t))\delta(t - t_{sp})$$

Here, U_{SE}' denotes the increase in value of U_{SE} with each spike, which follows the accumulation of calcium that is thought to underlie synaptic facilitation.[35] For LHN2, R_m was set to 4.1GΩ based on our experimental measurements and C_m was estimated at 12.5pF based on the neuron's size. The parameters τ_{rec} (the time constant of recovery from depression), τ_{facil} (the time constant of recovery from facilitation), τ_{rec}, U_{SE}', and A_{SE} were jointly optimized to minimize the mean squared error of each uEPSP amplitude, using the lsqcurvefit function of the MATLAB optimization toolbox.

For both LHN types, we fit the synapse model to the mean uEPSP amplitudes across trials and pairs because our goal was to model the average synaptic dynamics, not the variability of synaptic responses. The exact number of spikes was similar but not identical from trial to trial (both within pairs and between pairs). The 10 current pulses evoked a trial-averaged 71.5±8.9 DM1 spikes (mean

Current Biology
Article

 CellPress

±s.d.; n = 10 pairs), corresponding to a small amount of variability across pairs (CV = 0.12). The variability across trials within each pair was even smaller (CV = 0.024±0.017; mean±s.d.; n = 10 pairs). We therefore used only as many spikes per pulse as were present across all trials and recordings. For LHN2, this was 6 spikes for pulses 1-7 and 5 spikes for pulses 8-10. For LHN2, this was 7 spikes for the first pulse, 6 spikes for pulses 2-7, and 5 spikes for pulses 8-10. On average, this meant that 20% of PN spikes (all at the end of each current pulse) were excluded, so the model fits for the timescales of depression are likely slight overestimates. However, this small distortion was similar between LHN1 and LHN2 models.

Behavior analysis

Fly trajectories from video recordings were extracted using custom Python code and processed as in previous studies.[52] Briefly, fly positions (x, y) were extracted using SLEAP. We then fitted a Savitsky–Golay filter (fourth-order polynomial and window size of 21 points) over positions to remove measurement noise. The instantaneous velocities were computed by analytically differentiating the fitted polynomials.

We excluded any trajectories that had average speeds lower than 2mm/s (i.e., non-behaving flies) or were shorter than 16s (stimulus period duration). To remove behavioral side-effects of encountering the arena walls, we did not consider trajectories that encountered the arena side walls or that started within 10cm of upwind side of the arena.

For each trajectory, 5 behavioral parameters were computed: upwind velocity, crosswind velocity, rotational velocity, angular heading, and total speed. We focused our analysis on upwind velocity, since that most directly reflects odor attraction.[27] Crosswind velocity, rotational velocity, and total speed were all highest in UAS-Shibire control flies, were lower in the Gal4-only control flies, and lowest in the Gal4/UAS experimental flies (data not shown). Flies with an average upwind velocity of less than 2mm/sec and more than -2mm/sec during the initial 5Hz stimulus were excluded from all analysis. To compute the "high-intensity surge velocity, the average velocity over a 400 msec window starting 300 msec after the switch to 10Hz stimulation was subtracted from the average velocity over a 500 msec window ending just before the switch to 10Hz stimulation. To compute the "low-intensity maintenance" velocity, the average velocity over the last 2 seconds of 2.5Hz stimulation was subtracted from the average baseline (no stimulus) velocity.